LICENTIATE THESIS

Spectral analysis in laser powder bed fusion

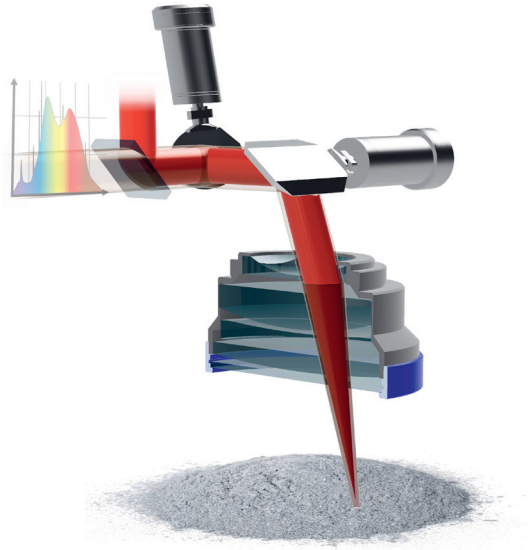

Benedikt Brandau

Manufacturing Systems Engineering

LULEÅ UNIVERSITY OF TECHNOLOGY

Licentiate thesis

Spectral analysis in laser powder bed fusion

Benedikt Brandau

Luleå University of Technology
Department of Engineering Sciences and Mathematics
Division of Product and Production Development
971 87 Luleå
Sweden

Luleå, May 2022

Printed by Luleå University of Technology 2022

ISSN: 1402-1757
ISBN: 978-91-8048-098-7 (print)
ISBN: 978-91-8048-099-4 (electronic)

Luleå 2022
www.ltu.se

Preface

In this licentiate thesis, I present work that I have done in the Manufacturing Systems Engineering group at Luleå University of Technology and in the System Development Advanced Manufacturing group at JENOPTIK Optical Systems GmbH as part of my PhD.

I would like to take this opportunity to express my gratitude to all those who have supported me during my work. This work and experience would not be the same without them.

I would like to thank my supervisors Frank Brückner and Alexander Kaplan for their support and for helping me to constantly improve my scientific thinking and my work. I am also very grateful to them that I can do my PhD in an industrial environment.

Thanks to all colleagues in Luleå as well as Frank's colleagues in the Additive Manufacturing Business Unit, Fraunhofer IWS for all the provided support and discussions.

I am very thankful for my old and new colleagues, who were always open for academic as well as private discussions and kept my back free for my PhD. A big thank you goes to my former team at Connected Optics and especially to the group leader Jan Werschnik, who gave me the opportunity to do an industrial PhD at JENOPTIK. Their advice, support and valuable comments have always inspired me to think in new ways.

Special thanks are to be given to my family, friends and especially my fiancée, for her support in all circumstances.

Benedikt Brandau
Luleå 2022

Abstract

This thesis is about the investigation of the spectral interaction of electromagnetic radiation with metal powders. For this purpose, spectral data of powders for laser powder bed fusion processes are investigated in three papers using different techniques. In paper A the spectral radiation behavior of the laser interaction zone is considered, in paper B and C the absorbance behavior of different metal powders depending on their state and measurement method.

Paper A investigates the spectral signal of the process light generated by laser material interaction in laser powder bed fusion. The detection is performed by a coaxially guided measuring beam and a quasi-coaxial measuring beam simultaneously guided by another scanning optics. The signal characteristics depend on the angle of incidence of the measuring beam to the laser material interaction zone. Using high-speed recordings and optical simulations, a model for describing the signal behavior could be determined. The measured spectral intensity distribution representing the degree for energy coupling can be corrected with a correction factor over the whole field for solid materials. This correction includes a function describing the numerical aperture of the measuring channel and the laser intensity on the working field. For the investigated powder, the measurement signal fluctuated strongly and no transferable model could be formed. The reason for this was the different absorbance behavior of the powders investigated. **Paper B** therefore deals in detail with the spectral absorbance behavior of metal powders for additive manufacturing. Using a high-precision spectrometer, 39 powders were measured reflectively over a wide spectral range and the absorbance determined. By varying the degree of use, aging, grain size and impurities, various influence parameters are determined experimentally and discussed theoretically. Based on 20 derived laser wavelengths, technically usable wavelengths with better process efficiency and stability are proposed. From the obtained absorbance, the efficiency of energy coupling can be estimated and forms a broad data base for the optimization of laser parameters. In order to perform the absorbance determinations also in situ in a laser powder bed fusion system **paper C** describes a possibility of an inline absorbance determination by high resolution coaxial imaging. A method is discussed for geometrically correct and gapless imaging of the processing plane, recorded through the laser optics. By imaging at six different wavelengths, metal powders can be distinguished by their absorbance spectrum and impurities can be detected. In an experimental implementation the functionality of the method is proven. The results are validated by optical simulations, ray tracing and comparative measurements with a high-precision spectrometer.

List of Publications

The main part of the licentiate thesis is composed of the following three papers, included in the Annex:

A: Angular dependence of coaxial and quasi-coaxial monitoring systems for process radiation analysis in laser materials processing
Benedikt Brandau, Torsten Mai, Frank Brückner, Alexander F. H. Kaplan
Published in Journal of Optics and Lasers in Engineering, 155 (2022) 107050.
10.1016/j.optlaseng.2022.107050

B: Absorbance study of powder conditions for laser additive manufacturing
Benedikt Brandau, Adrien Da Silva, Frank Brückner, Alexander F. H. Kaplan
Published in Journal of Materials & Design, 216 (2022) 110591.
10.1016/j.matdes.2022.110591

C: Proof-of-concept of an absorbance determination of a powder bed by high resolution coaxial multispectral imaging in laser material processing
Benedikt Brandau, Frank Brueckner, Alexander F. H. Kaplan
Submitted to a journal in May 2022

Additional conference publication by the author, not included in the thesis:

Design aspects of monitoring systems in laser powder bed fusion (LPBF)
Benedikt Brandau, Frank Brückner
Proceedings of Thuringia Material Days 2021, Weimar, Germany, July 2021

Publications as co-author, not included in the thesis:

Influence of build geometry and powder aging on the degradation of AlSi10Mg powder in laser powder bed fusion

Tatiana Fedina, Filippo Belelli, Giorgia Lupi, Benedikt Brandau, Riccardo Casati, Raphael Berneth, Frank Brueckner, Alexander F. H. Kaplan
SSRN (2022) 10.2139/ssrn.4074939

Influence of aluminium powder aging on directed energy deposition
Adrien Da Silva, Filippo Belelli, Giorgia Lupi, Francesco Bruzzo, Benedikt Brandau, Lukas Maier, Alexander Pesl, Jan Frostevarg, Riccardo Casati, Elena Lopez, Alexander F. H. Kaplan
Materials & Design, 218, (2022) 110677 10.1016/j.matdes.2022.110677

Author's contribution to the publications

Paper A: Planning & performing experiments; experimental setup construction; literature study; acquiring high-speed imaging footage; acquiring spectroscopic measurements; sample preparation; acquiring surface images; quantitative analysis of high-speed videos & surface images; interpretation of results in relation to state-of-the-art; optical simulations; creating all figures included in the paper; writing the paper & discussions with co-authors to improve the paper.

Paper B: Planning & performing experiments; acquiring spectroscopic measurements; literature study; sample preparation; qualitative & quantitative analysis of absorbance spectra; interpretation of results in relation to state-of-the-art; creating all figures included in the paper; writing the paper & discussions with co-authors to improve the paper.

Paper C: Planning & performing experiments; experimental setup construction; literature study; acquiring spectroscopic measurements; optical simulations and ray tracing; acquiring coaxial absorbance measurements; acquiring surface images; interpretation of results in relation to state-of-the-art; creating all figures included in the paper; writing the paper & discussions with co-authors to improve the paper.

Abbreviations

AM	Additive manufacturing
AOI	Angle of incidence
AR	Anti-reflective
BWD	Back working distance
DED	Digital mirror device
DLP	Digital light processing
DMD	Digital mirror devices
FS	Fused silica
FSM	Fast steering mirrors
HAZ	Heat affected zone
HSI	High speed imaging
HR	High-reflective
IR	Infrared
LBPF	Laser powder bed fusion
LIDT	Laser induced damage threshold
LIBS	Laser induced breakdown spectroscopy
PoOS	Post-objective scanning
PrOS	Pre-objective scanning
SLA	Stereolithography
USP	Ultra short pulse
UV	Ultraviolet
VIS	Visible
YAG	Yttrium aluminum garnet

List of Symbols

Δz_G	Degree of defocusing for Gaussian beam
Δz_T	Degree of defocusing for tophat beam
A_D	Entrance pupil diameter
A_p	Position of the entrance pupil
D_{EB}	Entrance beam diameter
D_F	Scan field diameter
D_S	Focus diameter
E_0	Fundamental energy level
E_1	Excitation energy level
E_p	Photon energy
I_L	Laser intensity
$M_{Ge\lambda}$	Specific spectral radiation of a grey body emitter
$M_{e\lambda}$	Specific spectral radiation
R_p	Parallel polarized part of reflection
R_s	Perpendicular polarized part of reflection
T_e	Electron temperature
T_t	Temperature
c_0	Speed of light in vacuum
d_1	Distance mirror 1
d_2	Distance mirror 2
d_s	Layer thickness
g_m	Number of degenerate energy levels
k_1, k_2	Constants
n'	Real part of complex refractive index
n_{AR}	Refractive index of anti-refelection coating
n_m	Refractive index of the adjacent medium
n_s	Refractive index of the substrate
λ_{max}	Wavelength of the maximum spectral intensity
ϵ_T	Emission coefficient
E_m	Emission energy
Δz	Degree of defocusing
h	Planck constant
σ	Angle of incidence
σ'	Angle of reflection
A	Absorption
AD	Resolving capability
C	Surfaces curvature

F	Scan field position
I	Spectral intensity
L	Deviation of the position of the entrance pupil
P	Laser power
R	Reflection
T	Transmission
VD	Spectral resolving capability
c	Speed of light in medium
d	Glass thickness
f	Focal length
ik	Imaginary part complex refractive index
k	Boltzmann constant
n	Refractive index
x, y, z	Field coordinates
Ψ	Absorption coefficients for the coating
Ω	Absorption coefficients for the glass
α	Thermal expansion coefficient
β	Half of the aperture angle
γ	Heat conduction coefficient
ε	Permittivity
ζ	Aposidation factor
θ	Scan angle
λ	Wavelength
μ	Permeability
ν	Frequency
ρ	Transition probability
τ	Lifetime of the energy level
φ	Mirror angle

Contents

Introduction

1. Organisation of the thesis

An introduction is provided to introduce the papers and to clarify the relationships between them. The main part of this thesis consists of three papers, which are attached in the annex.

In the introduction to this thesis, the motivation and the significance of the research are clarified (section 2). Some basics, which are beneficial for the understanding of the paper, are given in section 3. This includes the components and operation of scanner optics (paper A and C), spectral interaction processes in laser material processing (paper A) and fundamentals of the interaction of electromagnetic radiation with materials (paper B and C). Then, the different methods and tools used in the work are briefly discussed and evaluated (section 4). Section 5 gives a brief overview of the abstracts and main results of papers A-C. The overall conclusion of this work is given in Section 6 and an outlook in Section 7.

The main aspects of the three papers are shown in table 1. In **paper A**, the spectral characteristics of the process light generated by the laser material interaction are investigated. For this purpose, a concept of a quasi-coaxial measurement setup was demonstrated, in which signals could be recorded in the complete working area in the wavelength range of λ = 300 - 3400 nm without the influence of transmitting optical components. A correlation was found between the spatial orientation of the monitoring system and the angular ratio of the measuring and processing beam. A process zone that changes with the angle of incidence could be detected via high-speed recordings. Using optical simulations of the measuring and laser optics, a model could be formed, whereby the angle and measuring system influences could be corrected. It turned out that the main influence of the spectral expression of the process light lies in the intensity variation caused by the laser optics. If the absorbance of the material to be processed is known, it can be used to obtain information about the coupled laser energy. In order to generate a broad data set of absorbance values as a basis, the absorbance of metal powders for additive manufacturing was determined in **paper B** using a high-precision dual-beam spectrometer. A broad wavelength range of λ = 330 - 1560 nm was investigated and 20 laser wavelengths were derived from this. In order to provide a broad data base, values for: steels, aluminum alloys, titanium alloys, Nitinol, high entropy alloy, chromium, copper, brass and iron ore were recorded. The materials could be clearly differentiated by their absorbance spectrum, and differences between grain sizes, aging and use states were visible. Since the measurements are very time consuming and may not describe the state of the powders in the

machine, a concept was developed in **paper C**, which allows the determination of the absorbance in a powder bed fusion machine. This concept includes a coaxial imaging of the processing surface at different wavelengths and a derivation of the absorbance from the gray values of the images. Thus, absorbance differences can be detected geometrically correct in the complete build area and evaluated via imaging. This allows absorbance differences in the powder caused by foreign particles, impurities, oxidation or spatter to be detected. The technical proof was achieved experimentally with 20 different powders and verified by optical simulations, ray tracing and spectrometer measurements.

***Table 1** - Thematic overview of the papers*

Topic	Paper A	Paper B	Paper C
Absorbance spectroscopy		x	x
Coaxial imaging	x		x
Emission spectroscopy	x		
High speed imaging	x		
Laser welding	x	x	x
Optical simulation	x		x
Powder conditions		x	x
Ray tracing		x	x
Scanning optics	x		x

Through the research from the three papers, it is possible to create a monitoring concept for a laser powder bed fusion machine, with which the welding process, the powder, the coating blade and the workpiece can be monitored or the laser, scanner and printing strategy can be controlled. The cover page illustrates the concept of such a system and shows the three measurement strategies of this thesis.

2. Motivation of the research

Additive manufacturing (AM) is very lucrative in prototyping. For example, AM reduces the time and cost from the design phase to production by eliminating the need to invest in the design and manufacture of the necessary tools and fixtures. Laser powder bed fusion (LPBF) technology is becoming a market leader in industrial manufacturing due to its low post-processing requirements, high accuracy and component quality [1,2]. It also enables new ways of thinking in the design of components. Despite the large projected market growth of 14.32 % by 2024 [3], the step to complete industrialization has not yet been reached. A major problem lies in process know-how and the variety of possible manufacturing errors [4]. With printing times of one day up to weeks, a work piece defect means enormous economic losses. For this reason, technologies for process monitoring up to self-regulation of print jobs are the most promising research focus in order to make LBPF more sustainable and industrially ready [5,6].

There are already several machine concepts or research work on monitoring strategies, and many processes are now established in commercial systems [6]. However, there are still many unexplored phenomena and interactions that lead to component defects. This thesis will explore new possible optical techniques for AM (paper A and C), investigate phenomena of laser material interactions (paper A) and discuss principles of measurement techniques (paper B). In cooperation with JENOPTIK, which as an original equipment manufacturer produces many core components for laser material processing machines, the results of this work will influence optics or machine designs. Optics for beam guidance, beam manipulation and beam shaping can then be specifically designed regarding monitoring.

The work was done in collaboration with Lulea Technical University, Fraunhofer Institute for Materials and Beam Technology and JENOPTIK Optical Systems GmbH.

3. Technological and scientific background

In the following chapters of this thesis, the theoretical basis for the aspects and methods discussed in the three papers will be introduced. This includes design criteria for optical components of laser material processing and fundamentals of laser material interaction. The different possibilities of process monitoring are not further described in the introduction. A comprehensive research on this topic can be found in the attached papers A and C.

3.2 Laser- material interaction

Albert Einstein established the cornerstone for major revolutionary innovations in many scientific fields and especially in manufacturing technology in 1917 with his publication: "The Quantum Theory of Radiation". He described for the first time that in addition to the known emission by relaxation of thermally generated electrons, as for example in filament bulbs, spontaneous and stimulated emission also exist [7].

In the following years it was shown that it is possible to induce a discrete emission by a present radiation field [8]. This led to the development of laser technology [9]. Where laser is an acronym and stands for "light amplification by stimulated emission of radiation". The term laser has too become established as the name of a device that emits coherent radiation. Compared to thermal relaxation emission sources, a laser offers the advantages of high monochromaticity and spectral energy density. In addition, it has a large temporal and high spatial coherence and the generation of very short light pulses is as well possible [10]. The elementary basic mechanism that enables these advantages is the external excitation of an atomic system and the emission of discrete electromagnetic waves when it falls back to the lower-energy state. The frequency condition with frequency ν, the Planck constant h, the fundamental energy level E_0 and the excitation level E_1 applies (equation 1).

$$E_1 - E_0 = h \cdot \nu \qquad \text{Equ. 1}$$

Furthermore, an electromagnetic wave with the propagation speed c_0 and the wavelength λ in vacuum can be described by the simple relation from equation 2. Thus, by means of the frequency condition, a statement about the energy E_1 required for the excitation is made, which must be greater than or equal to the photon energy E_p (equation 3).

$$c_0 = \nu \cdot \lambda \quad \text{Equ. 2}$$

$$E_1 \geq E_p = h \cdot \nu = \frac{h \cdot c_0}{\lambda} \quad \text{Equ. 3}$$

The aim is to obtain a population inversion by adding energy, which is called "pumping", to the stimulation energy [11]. A population inversion is achieved when a larger population density occurs in the energetically higher, than in the energetically lower levels. The excitation can be achived optically by flash tubes, LEDs or other lasers, but also by a current flow or impulse excitation [11,12]. If there is a population inversion in the system after the excitation, the reversion to an energetically lower level can be induced by another external action. This process is known as stimulated emission. Materials that are capable of this are called laser-active media. This can also be divided into three groups [12]. Gas phase lasers such as excimer or noble gas lasers, diode lasers based on semiconductors and the solid state lasers. In the case of the latter, the laser-active medium is in the form of a fiber, a disk or a rod. By doping the base material, wavelengths from the visible (VIS) to the infrared (IR) spectrum can be covered. Examples of laser active media for solid state lasers are Ti:sapphire, Nd:YttriumAluminumGarnet (YAG) or Yb doped glass fibers. Ytterbium fiber lasers with a central wavelength of λ = 1070 nm are the most commonly used laser source in LPBF systems [13]. In general, the advantage of solid-state lasers is their long lifetime together with the high achievable power. Therefore, solid-state based lasers are preferably used in industrial laser material processing [14,15].

In the following, some laser material interaction processes are described, which form the basis for material processing and process monitoring.

3.2.1 Transmission

When laser radiation hits a medium, the electron system and the atomic network interact with the photons [16]. The lossless propagation of radiation in a medium is known as transmission. This occurs when the band gap is greater than the photon energy of the laser. This is known as transparency of the medium to the spectrum. In laser technology, the mechanism of transmission finds its main application in optical elements for beam delivery and beam shaping [17,18]. Typical materials are optical glasses, because the band gap of most glasses is larger than the photon energy of visible light.

Hence, light propagates in a vacuum at the constant speed of light c_0 regardless of its wavelength, while the speed of light in a medium, such as a glass, assumes a value $c < c_0$. A beam of light is an electromagnetic wave and can be simplified by describing the propagation of light as a transversely limited plane wave [19,20]. An electromagnetic wave is built up from a superposition of an electric wave and a magnetic wave perpendicular to it with the same direction of propagation [20]. Therefore, photons interact with the electric and also magnetic fields of matter. The propagation velocity in a medium can be determined with an extension of equation 2 with the permittivity ε and the permeability μ (equation 4) [21].

$$c = \frac{1}{\sqrt{\varepsilon\mu}} \cdot \nu \cdot \lambda \qquad \text{Equ. 4}$$

$$n = n' + ik \qquad \text{Equ. 5}$$

$$n = \frac{c}{\nu \cdot \lambda} = \sqrt{\varepsilon\mu} \qquad \text{Equ. 6}$$

During the transition of a light beam between optically different dense media, a change of the propagation speed and of the propagation direction as well occurs. This process is called refraction and is described by the dimensionless refractive index n. The refractive index is composed of a real part n' and an imaginary part of a complex number ik (equation 5). The refractive index is also proportional to the root of the permittivity and permeability and directly dependent on the frequency and wavelength used. Equation 6 shows that different wavelengths are refracted to different degrees [22].

The wavelength dependence of the refractive index is called dispersion. Dispersion describes the frequency- and substance-dependent propagation speed of electromagnetic waves in a medium [16]. Since permittivity and permeability are temperature-dependent, media with different temperatures also have different dispersion and refraction behavior. Thus, an optical system made up of the same glasses at different temperatures in addition shows different imaging properties [23]. To describe the dispersion of different glasses in the visible range, the dimensionless Abbe number ν_A was introduced as a material parameter.

3.2.2 Absorption

Interactions of photons in a transparent medium can still occur. This is the case at high intensities as in high-power lasers or ultrashort pulse lasers (USP) in the form

of nonlinear multiphoton processes [24]. Here, due to the high photon density, several photons can interact simultaneously with one electron [25].

For example, two photons hit an electron simultaneously and the energy is adequate to lift the electron from the ground state to a higher energy level [26]. The result is the absorption of the two photons [25,26].

However, the simplest case is the linear absorption process. This occurs when the energy of the photons is greater than the band gap of the medium. The energy is transferred to an electron, which thereby changes to a higher energy state within its atom. In this case, the conservation of energy applies, which means that a corresponding level with the appropriate energy difference must exist in the atom. Electrons can therefore change from the valence band to the conduction band. Unbound electrons have a very strong interaction with electromagnetic radiation. Here materials, such as metals, have largely no transparency. If the photon energy from parts of the visible spectrum is equal to the band gap energy, the material has a color. The energy absorbed by the electrons can be re-emitted in the form of radiation or as a non-radiating transition, phonons. The latter lead to a heating of the material [27].

The emission of photons can be described analogously to absorption. An excited electron will always relax back to its ground state. For this, it must emit energy. The energy E_m lies between the two energy states E_0 and E_1, as shown in equation 7.

$$E_m = E_1 - E_0 \qquad \text{Equ. 7}$$

The wavelength of the emitted photons is very strongly element-dependent. Conversely, the absorption is also strongly dependent on the wavelength and the chemical composition of the material. Therefore, different materials exhibit specific absorption spectra. By measuring emission and absorption spectra, the elemental composition of materials can be determined.

Metals form three absorption categories due to their energetic structure [28–30]. Exemplary absorption spectra for the three categories can be found in figure 1.

Transition metals are characterized by a constant decrease in absorption with increasing wavelength. Typical elements are iron and titanium.

Multivalent metals, e.g., aluminum and magnesium, exhibit low absorption over the entire wavelength range, except for sporadic interband transitions. These interband transitions are triggered by the absorption of a photon.

The third category, noble metals such as gold or copper, show constant low absorption in the near and far infrared regions, but a significant increase in the visible region of the wavelength spectrum. This can be explained by relativistic effects of the electron orbitals. The higher number of atomic charges increases the electrostatic attraction of the atomic nucleus to the electrons. The s orbitals contract and the p orbitals expand, resulting in a smaller band gap. The resulting energy difference corresponds to the wavelength of the absorbed light. In copper, for example, high-energy blue to green photons are absorbed, leading to electron transitions. The red spectral range, on the other hand, is reflected, resulting in the reddish shine.

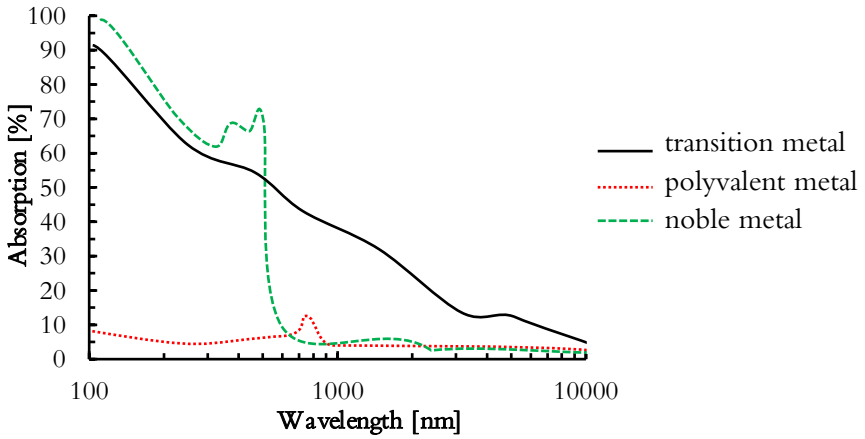

***Figure 1** - Comparison of exemplary absorption spectra of transition, polyvalent and noble metal.*

3.2.3 Reflection

Besides absorption and transmission, the last mechanism is reflection. In this process, a photon interacts with an electron or an atom in the material, from which it is absorbed and immediately re-emitted. The resulting effect of this process is called reemission and is what is noticed as reflection. [24]

In classical electrodynamics, the incoming photon can be assumed to exhibit wave-like behavior due to wave-particle duality [31]. As already describes, the waves consist of a magnetic field and an electric field [20]. The oscillating electric field of this wave interacts with the atomic structure when it hits a medium and polarizes the atomic dipoles. It causes the dipoles to shift slightly and to oscillate. Due to the oscillation, the dipoles emit electromagnetic radiation with the same frequency of the excitation wave. By the Huygens-Fresnel principle it is known

that this emission is a spherical elementary wave, which originates from any point hit by a wave front [32]. The wave front is perpendicular to the passing light beam and is a point of the same phase. The elementary waves interfere with each other and form a new wave front in the same plane and angle to the normal as the incident wave front. Thus, the angle of incidence (AOI) σ is equal to the angle of reflection σ', and the law of reflection (equation 8) applies [32].

$$\sigma = \sigma' \qquad \text{Equ. 8}$$

An additional wavefront extends into the material and forms the transmitting beam. Further propagation of a wavefront in other directions is not possible due to interference-induced annihilation. Due to the unbounded electrons in metals, the probability of photons interacting with the electrons is very high. For this reason, all metals have a very high reflectivity for large parts of the spectrum. For a more detailed consideration, Fresnel's formula must be used [33]. For the angle of incidence σ the reflection of the parallel polarized part (R_p) can be described with equation 9. Here n' is the real part and ik is the imaginary part of the complex refractive index. For the perpendicular polarized (R_s) component equation 10 applies. P-polarized light is the portion where the magnetic field of the electromagnetic wave is perpendicular to the plane of incidence. S-polarized light, on the other hand, is the portion where the electric field is perpendicular to the plane of incidence [34]. The complete reflection is given by the superposition of R_s and R_p from equation 11.

$$R_p = \frac{\left(n'^2 - \frac{1}{\cos\sigma}\right)^2 + ik^2}{\left(n'^2 + \frac{1}{\cos\sigma}\right)^2 + ik^2} \qquad \text{Equ. 9}$$

$$R_s = \frac{(n'^2 - \cos\sigma)^2 + ik^2}{(n'^2 + \cos\sigma)^2 + ik^2} \qquad \text{Equ. 10}$$

$$R = R_p + R_s \qquad \text{Equ. 11}$$

Reflection occurs at a material transition with a refractive index difference. The reflection depends on the refractive index of the output medium n_1, on the refractive index of the input medium n_2, on the polarization of the radiation and on the angle of incidence σ. A special case plays the normal incidence, which allows the simplified calculation of the reflection R (equation 12).

$$R = \frac{(n_1 - n_2)^2}{(n_1 + n_2)^2} \qquad \text{Equ. 12}$$

The relationship as well as the proportion of transmission T, absorption A and reflection R can be generally described by equation 13.

$$R = 1 - (T + A) \qquad \text{Equ. 13}$$

On technical surfaces, such as a powder surface, a single beam can be reflected several times (figure 2) [35,36]. The sum of the individual reflection processes is known as reflectance. With each reflection, a portion of the light is also absorbed. Therefore, the more reflections occur the more the sum of the absorption increases (absorbance). On an ideal surface and on the top of the particles (1 and 2) the light reflects directly. However, multi-reflections between different particles (3) and complete absorption can occur if the beam is trapped (4). The consequence is that the effective part of the light reflected from the surface is lower than in the case of an ideal surface [35,36].

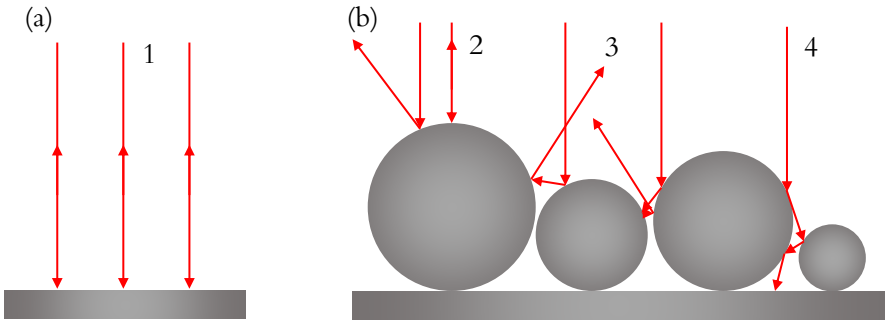

***Figure 2** - Comparison of the reflection of an (a) ideal surface with a (b) technical surface based on the example of a powder. 1 and 2 shows the direct reflection, 3 show a multi-reflection, and 4 a beam trap.*

3.3 Laser material processing

3.3.1 Laser melting and welding

In industrial production, laser welding has become established as joining technology due to the good properties of the produced weld seam [37]. On the one hand, there is the possibility of a large aspect ratio, on the other hand, the heat affected zone (HAZ) is very small compared to other welding processes [38]. Furthermore, there is no wear of the tools, such as electrodes or nozzles. Furthermore, laser welding has a very high automation potential and is nowadays mostly carried out completely automatically [39]. Thus, the processing speed of

materials can be greatly increased with the help of laser applications, which leads to better cost efficiency in production [39].

With a suitable selection of the laser source, most of the energy is absorbed as described in the previous theory. The energy absorbed locally at the material surface is conducted into the material in the form of heat [40,41]. This leads to melting and, in some applications, to vaporization of the material. Convection causes mixing of the molten material and after cooling a weld is formed [42]. Depending on the material to be welded, the melting zone is protected by a shielding gas. This prevents oxidation of the molten material [43,44]. Depending on the laser intensity I_L used, a distinction is made between heat conduction welding (typically $I_L < 106$ W/cm^2) and deep penetration welding (typically $I_L > 106$ W/cm^2) [12].

In heat conduction welding, the material is heated locally to above its melting temperature and this heat is conducted non-directionally into the rest of the material. A radially symmetrical temperature gradient is created, resulting in a weld seam with a circular cross-section. However, due to the low intensity of the laser radiation and the resulting low energy input into the material, the welding depth is strongly limited in this application [45].

In comparison, for example aspect ratios of 10:1 [46] can be achieved in deep penetration welding. The radiation intensity of the laser is increased via the threshold intensity of the vaporization of the material. Due to the high laser intensity, not only a melt is formed, but also a vapor capillary is produced, which is known as a keyhole [12]. A cloud of metal vapor is emitted from the keyhole toward the top of the material [47]. The metal vapor is clusters up to single neutral metal atoms. Viewed from the outside, the metal vapor emits a continuous spectrum, similar to that of a light bulb. The laser radiation is absorbed in the generated metal vapor, so that the metal vapor heats up strongly. As the temperature rises, the emitted spectrum is shifted in the direction of the shorter wavelengths. Depending on the laser power, a laser-induced metal vapor plasma can result from direct absorption or in combination with impact excitation. A plasma is present when unbound electrons, atoms and ions are present simultaneously. Furthermore, plasma leads to an emission of discrete spectral lines which show a characteristic emission spectrum depending on the elements. Additionally, the plasma leads to a better coupling of the laser radiation into the melting zone and thus to a significantly higher absorbance compared to a solid material surface [48]. The vapor capillaries transfer the energy of the laser deep into the material. This allows deep welds to be produced. The energy is almost

completely converted into heat, as multiple reflections of the laser radiation within the keyhole cause it to be almost completely absorbed [46]. The result of the welding process depends on the formation and shape of the keyhole. The material is melted in the feed direction of the laser at the front of the keyhole. A part forms the melt, the rest is vaporized, but the proportions depend on the laser power [46]. When there is no more energy input by the laser, the keyhole collapses and solidification of the melt occurs.

3.3.2 Laser powder bed fusion

Laser powder bed fusion or also known as selective laser melting is based on layer-by-layer melting of a powdered material [49–51]. LPBF can be compared with laser joining. In this respect, the assumptions of laser joining can also be adopted, to a certain point, for LPBF [52]. The starting point is a 3D model and the layer model of the workpiece to be printed which is derived from it. The individual layers form the exposure masks, which are rasterized by a laser. Figure 3 shows the workpiece generation process in detail. First, a thin layer of the metal powder, from a powder reservoir is applied to the build platform by a powder application system. The powder application system can be a roller or a blade. The only important factor is the uniform layer thickness produced. The laser then melts the areas of the powder that were calculated according to the layer model at the corresponding material height. When melting the powder, the laser parameters must be selected in such a way that both the corresponding powder layer and part of the underlying already solidified metal layer are melted. This creates a solid part with theoretically absolute density [51]. Depending on the material, workpiece and scanning strategy, the use of a keyhole is necessary for this purpose, as this

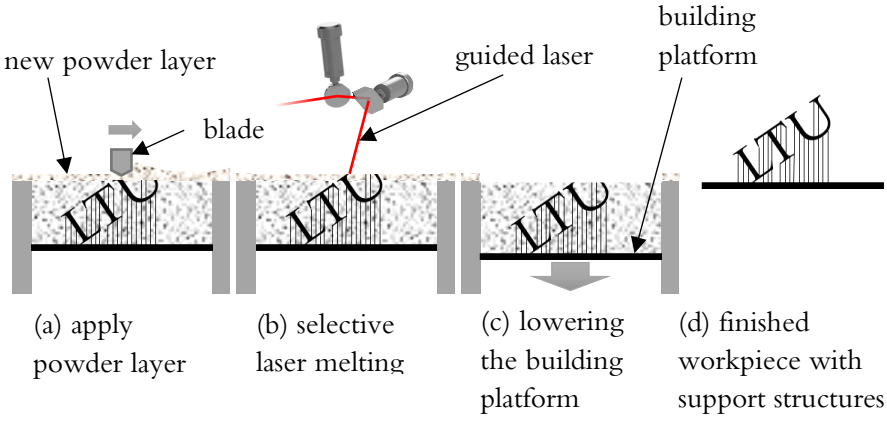

***Figure 3** - Simplified illustration of a laser powder bed fusion process. The processes steps (a) to (c) are repeated until the finished part (d) is produced.*

guarantees sufficient melting depths for the layer to bond to the entire component. During the melting process, attention must also be paid to the distance between the individual laser lines, the so-called hatch distance, so that the entire material is melted and thus closed surfaces are produced. Furthermore, attention must be paid to a uniform energy input into the powder bed in order to keep thermal stresses in the workpiece as low as possible. The thermal energy can be dissipated by already printed structures of the part or by support structures [49]. Also, the thermal input can be kept constant by adapted scan strategies, via a uniform sequential exposure over the entire powder bed [53,54].

In the next step, the build platform is lowered by the thickness of a layer and the entire process is repeated until the component is finished. The positioning of the laser on the powder surface is realized via a computer-controlled robotic arm with a processing head or a laser scanning system.

A brief description of the process can be found in the appended papers B and C.

3.4 Spectral process signals

Many variations of process monitoring have developed for laser welding and these can be applied to LPBF [55,56]. A broader overview of current research can be found in the attached paper C. In this thesis, the focus will be on the optical monitoring of the process or the feedstock. The spectral measurement and the determination of the absorbance spectrum of the powders with the associated theory are described in more detail in papers B and C.

In the following, some theoretical background will be clarified, on which the evaluation of spectral measured process signals is based. The theory that can be used to evaluate the laser material interaction in the process using the spectra recorded with the setup from paper A. For the evaluation, it is assumed that the excitation for the induced emission is thermal or optical, via absorption of the laser energy [57]. The radiation source can therefore be the melt, the metal vapor or also the plasma, which is generated by the laser material interaction. Depending on the excitation, material and laser intensity used, they emit a characteristic spectrum [58,59].

3.4.3 Emission line spectrum

The simplest spectrum is a line spectrum. It consists of one or more spectral lines. These can be emission lines or absorption lines which cut into an existing continuous spectrum. They are almost completely formed by transitions between discrete energy levels in the atom.

Thereby the width of the line is first given by the natural line width, due to the uncertainty principle according to equation 14. With a limited lifetime of the energy level τ with a photon energy E_p as in equation 3 a limited width of the spectral transition results by equation 15.

$$E_p \cdot \tau \geq h/2\pi \qquad \text{Equ. 14}$$

$$\Delta\nu \geq \frac{1}{2\pi \cdot \tau} \qquad \text{Equ. 15}$$

The natural line width is the minimum width that each spectral line owns. Furthermore, additional line broadening occurs due to temperatures and pressure [60]. At temperatures above 0K, thermal oscillations of the atoms occur and cause a broadening of the energy levels. The frequency of the emitted light is thus affected by a shift due to the Doppler effect [61]. In plasmas, a special case can occur, where the expected observed spectral lines are smaller or not measurable at all. This can be caused by self-absorption, where the radiation emitted by the relaxation is immediately absorbed by another electron in an atom [62]. The emitted energy must behave analogous to equation 3 from chapter 3.2.

In deep penetration welding line spectra are generated in laser induced plasma [63]. From knowledge of the characteristic atomic transitions, conclusions can be drawn about the qualitative and quantitative composition of the welded material. If the composition is known, the temperature of the plasma and therefore the energy introduced can be derived. One possible method is the determination of the electron temperature from the spectrum [63,64]. From this, the energy input into the material can be derived as a result of the formation of a plasma.

3.4.4 Spectral measurements of electron temperature

The requirement for determining the electron temperature is that free electrons are present. That is the case in a plasma. After the dissociation of the atoms, the lightweight electrons have more energy than the atomic nuclei. As a result,

thermal equilibrium within the vapor can no longer be assumed [64]. The result is a division into electron temperature, ion temperature and degree of ionization.

The comparison of the intensity of two spectral lines of an element is suitable for the calculation of the electron temperature [63–68]. The basis of the calculation of the intensity difference is given by equation 16. For this, the degenerate energy levels of the atom g_m, the transition probability ρ, the Boltzmann constant k and the wavelength λ, that is emitted during the transition, must be known [58,59,66]. The emitted energy E_m at the transition can be calculated analogous to equation 3 from chapter 3.2. The transition probability can be derived using Boltzmann statistics. The indices 1 and 2 stand for the spectral lines 1 and 2 selected for comparison.

$$\frac{I_1}{I_2} = \frac{\rho_1 \cdot g_{m_1} \cdot \lambda_2}{\rho_2 \cdot g_{m_2} \cdot \lambda_1} \cdot e^{-\frac{E_{m_1} - E_{m_2}}{kT_e}} \qquad \text{Equ. 16}$$

Rearranged, equation 16 can be used to directly determine the electron temperature T_e (equation 17).

$$T_e = \frac{E_{m_2} - E_{m_1}}{k \cdot \ln\left(\frac{I_1 \cdot \rho_2 \cdot g_{m_2} \cdot \lambda_1}{I_2 \cdot \rho_1 \cdot g_{m_1} \cdot \lambda_2}\right)} \qquad \text{Equ. 17}$$

The evaluation and monitoring of such a signal is not very computationally intensive, which speaks for the implementation in an in-situ monitoring [65]. In this case, the only thing that needs to be considered when selecting the lines, is that they are free of self-absorption [69]. If the spectral lines are constant over the entire process, the electron temperature is as well and homogeneous processing can be assumed. Fluctuations in electron temperature may indicate defects in the process due to too high or too low energy input [64]. This can cause voids, pores, inclusions and delamination of the single layers. If the process control does not allow such a high laser intensity that a plasma can form, other spectral signals must be used.

3.4.5 Countinuous emission spectrum

A continuous spectrum is composed of many individual emission lines. The distances between the lines go towards zero, so that they can no longer be distinguished from each other. Almost all measured spectra have a continuous component, but this can vary in intensity. Even with very narrow line spectra, a continuous background exists as error noise. Especially solids show a continuous

emission spectrum [70]. Responsible is a multitude of different effects [71]. Because of the high density of atoms within the solid, the electron shells of the atoms overlap and broad energy bands are formed instead of discrete independent levels. This increases the number of transitions allowed. Defects in the lattice structure result in further transition possibilities between the energy bands. Furthermore, phonons occur in solids. They are the reason for a continuous spectrum in the infrared region. If the temperature of the material increases, the spectrum shifts to shorter wavelengths. This phenomenon is known as thermal radiation [72].

The intensity and shape of this signal can be described by Planck's law of radiation (equation 18) [72].

$$M_{e\lambda} = \frac{k_1}{\lambda^5}\left(\frac{1}{e^{k_2/\lambda T_t} - 1}\right) \quad \text{Equ. 18}$$

$$k_1 = 2\pi \cdot h \cdot c_o^2 \quad \text{Equ. 19}$$

$$k_2 = \frac{h \cdot c_0}{k} \quad \text{Equ. 20}$$

The specific spectral radiation $M_{e\lambda}$ depends on the vacuum light speed c_0, the Planck constant h, the temperature T_t and the wavelength λ of the emitted photon. The constant k_1 can be determined by equation 19, the constant k_2 by equation 20.

However, that is only valid for a black body emitter (emission coefficient $\epsilon_T = 1$). Real bodies have an emission coefficient which can be much smaller and depends on influences like angle of incidence, angle of radiation, wavelength and surface condition [73]. For real bodies, a further simplified assumption can be made as gray body emitters. Here ϵ_T can be applied as an independent constant [73]. The specific spectral radiation $M_{Ge\lambda}$ results in the case of a gray body emitter by a multiplication of the emission coefficient ϵ_T with $M_{e\lambda}$ according to equation 21.

$$M_{Ge\lambda} = \epsilon_T \cdot M_{e\lambda} \quad \text{Equ. 21}$$

3.4.6 Temperature measurements via gray body emitter

Assuming that the process under consideration behaves like a gray body emitter, the emission spectrum of the material can be measured in order to determine ϵ_T. The spectrum chosen should be taken to be close to that of a known phase

transformation. The process can be recognized in the melting of the material or, in the case of evaporation, at characteristic spectral lines in the spectrum. In the case of the latter, these lines only have to occur sporadically and do not have to have a particularly significant intensity. In the next step, equation 21 is fitted to the measured spectrum. Since the temperature of the material is known as the melting or evaporation temperature, the only variable left is ϵ_T. Using ϵ_T as a fitting parameter, it can be utilized to determine the specific spectral emissivity for any given spectrum. From the emissivity spectrum of the gray emitter, the temperature can be derived via Wien's displacement law [74]. This results in an inverse proportionality between the temperature and the wavelength of the maximum spectral intensity λ_{max} (equation 21). By rounding the constants, a very simple formula for the estimation of temperature or maximum spectral intensity wavelength is given (equation 22).

$$\lambda_{max} T_t = \frac{h \cdot c_0}{4{,}966 \cdot k} \quad \text{Equ. 21}$$

$$T_t \approx \frac{3000}{\lambda_{max}} \quad \text{Equ. 22}$$

In this way, the temperature of the laser material interaction can also be derived from a continuous spectrum [63,75]. A statement about the melt pool temperature, penetration depth and the energy input are possible [76]. Technically, this can be realized in process monitoring in a simplified way using pyrometers. Depending on the design, they measure the intensity of one or two spectral ranges and evaluate these via the gray body emitter behavior [77]. However, knowing the exact material and ϵ_T is a requirement. Another difficulty is measuring the signals in the system, which usually deviate from the laser wavelength. Since the optical components in the laser powder bed fusion systems are primarily optimized for the laser.

3.5 Laser system components

3.5.1 Laser scanner

The core of every laser powder bed fusion system is the element for positioning the processing beam on the powder bed. In addition to a fixed optics which moves laterally along the x-y-axis and scans over the powder bed, the use of a 2D scanner with movable mirrors has established itself industrially [78]. These

scanners consist of two mirrors moving rotationally around one axis, that deflect the laser beam over the material surface. In the beam propagation direction, the laser beam first hits mirror 1, which rotationally deflects the beam onto mirror 2. Mirror 2 is typically oriented with its axis of rotation normal to the axis of rotation of mirror 1. The constellation allows a deflection in a direction normal to the first deflection direction. The mirrors have significantly smaller masses than an entire processing head. This allows very high dynamics and thus increased process speed [78]. Further advantages are the small footprints and the low maintenance. Technically, there are two scanner principles that have become established in laser material processing.

The faster polygon scanners (figure 4 b) [79], due to their fixed process direction (scanning only in x or y direction), only find applications in LPBF in some research work at present [80,81]. In these scanners, mirror 1 (laser side) consists of a polygon rotating at high and constant speed. This creates a scanning motion in a defined spatial direction. The beam deflected by the polygon hits a significantly slower mirror 2 (workpiece side) suspended on a galvanometer motor. That's leads to the second deflection of the beam. Due to the constant process direction, material buildup occurs in the LBPF at the end of the scan path. In addition, the surface quality of the components decreases, since no closed contours can be scanned. This type of scanner is preferably used for processing semiconductors, such as structuring solar cells or exposing printed circuit boards [82].

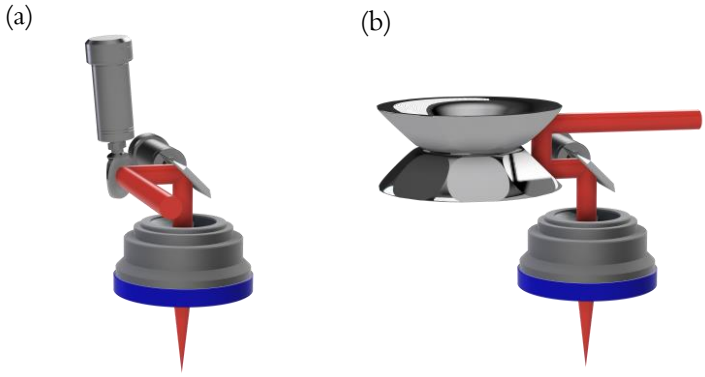

***Figure 4** - Schematic representation of (a) x-y-axis galvanometer scanner and (b) polygon scanner.*

In the LPBF, on the other hand, a scanner principle consisting of two mirrors moved by galvanometer motors has become established (figure 4 a). A deflection of the beam is possible in the scan field without gaps and with the same speed in both spatial directions.

As with polygon scanners, the galvanometer scanner with two different rotation points for the x and y deflection causes so-called image field distortion [83]. This pincushion-shaped image distortion is caused by the different distances between the mirrors and the plane in which the laser beam is deflected (figure 5). The distance between mirror 1 and mirror 2 depends on the scan angle. A larger scan angle leads to a larger distance between the mirrors, whereas the distance of the second mirror to the image field plane remains constant. The result is a different ratio of the two distances and a varying effect of the angle φ_1. Hence, the movement of one mirror does not lead to a rectilinear movement of the spot in the focal plane when the second mirror is constant. Consequently, an identical angle for mirror 1 (x-axis) and mirror 2 (y-axis) leads to an unequal amount of deflection on the image field. Thus, the distance F traveled is proportional to the focal length f and the tangent of the scan angle θ (equation 23), whereby the scan angle results from the deflection angle of the mirrors (equation 24) [12,83]. The scanning speed of the laser beam on the image field is affected by that, too. It is not directly proportional to the angular speed of the respective mirror. The

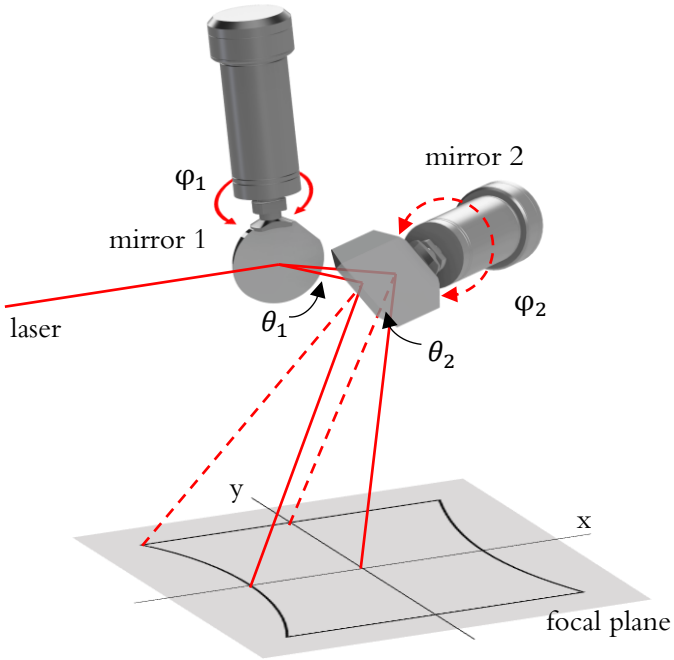

***Figure 5** - Angular relationship of the mirrors of a 2-axis scanner with the pincushion image field distortion caused by the axis distances*

distortion of the image field increases with increasing distance between the rotation axes of the mirrors.

$$F_{(x|y)} = 2f \cdot \tan \theta_{(x|y)} \quad \text{Equ. 23}$$

$$\theta_{(x|y)} = 2\varphi_{(1|2)} \quad \text{Equ. 24}$$

The distortion error can be compensated for the most part by software using specific control of the scanner mirrors using so-called correction files (look up tables) [83]. For this purpose, the geometrically correct image field positions are linked with the corresponding scanner angles. Fast Steering Mirrors (FSM) or the much smaller digital mirror devices (DMD) are hardware alternatives [84,85]. In both systems, a mirror surface is caused to oscillate at a resonant frequency by piezoelectric or electromagnetic effects. Depending on the excitation, a deflection in x and y direction is thus possible simultaneously at the same center of rotation. Due to the resonance frequency, however, only points in the working field can be approached which lie on the path of a Lissajous curve. Another disadvantage is the currently low power stability. For this reason, they are currently only used experimentally in 3D printers based on stereolithography (SLA) and digital light processing (DLP) technology [86].

Widely used is the correction of pincushion-shaped image field distortion by the optics which are used for beam focusing as well [87].

3.5.2 Category I: post-objective scanning

Focusing is an important tool to achieve an increase in intensity at low cost. Beam focusers can be reflective, allowing high optical powers to be used, or transmissive. The latter devices have a simpler design and can be designed much more compactly. Scanning methods with beam shapers are divided into two different categories [88], which are currently used equally in LPBF systems. A visual comparison of the two systems is shown in figure 6.

In post-objective scanning (PoOS), the scanner unit is located between the beam focuser and the working plane. If a single-focused beam is deflected via the scanner, the fixed focal length and the rotational movement result in a focus position that describes a spherical surface. In addition, there is an additional three-dimensional distortion of the spherical surface due to the mirror spacing described in the previous chapter. This is compensated by a so-called optical z-axis, which

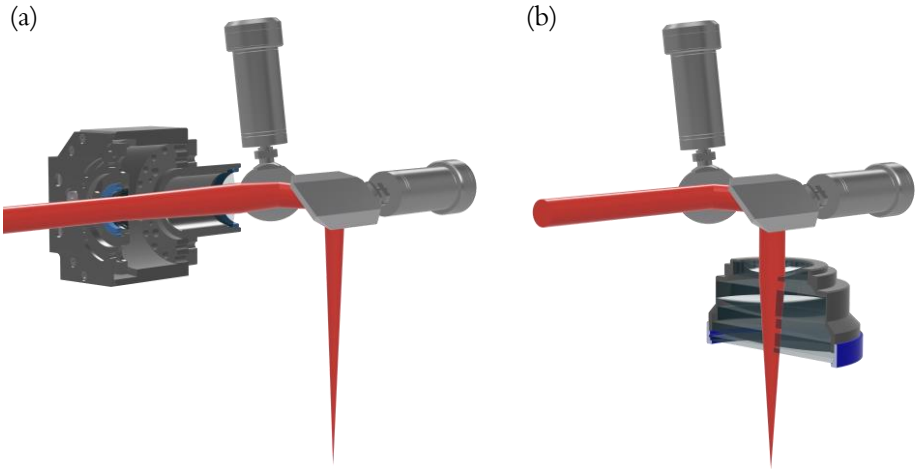

***Figure 6** - Schematic representation of (a) a post-objective scanning system with beam focusing via an optical z-axis (voice coil) and (b) a pre-objective scanning system with focusing via an F-Theta*

realizes the correction of the focus position typically by a focusing telescope arrangement. The z-axis is another active element. The axis has to be controlled simultaneously to the scanner. In the look-up table for the 2D field position, each 2D coordinate gets a third value for the z-position of the focus position. This transforms the actual curved focus position into the plane of the scan field. Constructively, this can be solved, for example, via a lens embedded in a moving coil actuator. By means of a moving coil in a static magnetic field, the coil can be positioned by applying a current [89]. Consequently, the movement of the lens causes a change in the focus position of the beam.

The advantage is a dynamically adjusted focus position, that allows angled or three-dimensional components to be machined without changing the setup [90]. It enables very large build-up field sizes, that can be derived trigonometrically from larger working distances. Temperature drifts in the form of focus shifts occurring during long machining operations can be corrected more easily, too [91]. By selective defocusing above or below the actual machining plane, the effective diameter of the laser spot on the workpiece can also be adjusted in the case of a Gaussian beam. Furthermore, PoOS systems are very well suited for process monitoring on wavelengths deviating from the laser. Due to the reflective beam deflection, there is no lateral chromatic color error.

The disadvantage is a decreasing dynamic range due to the mass of the moving lenses, which is usually limiting compared to the scanner. The component also requires more maintenance than passive optics. With large scan angles, there

is another disadvantage from a process point of view. Because of the variable deflection angle, paraxial ray of the output beam which are projected onto a plane is oblique to the optical axis. This is known as the angle of incidence (AOI) σ of the laser on the process plane. From a circular spot, an ellipsis is created with the long major axis oriented to the scan field center. Due to the different spot sizes and the distortion of the circle, an AOI-dependent laser intensity distribution is created. This can lead to a non-constant process, such as a different formation of the melt pool or keyhole. With increasing AOI, the penetration depth of the keyhole decreases in response to the decreasing laser intensity (figure 7).

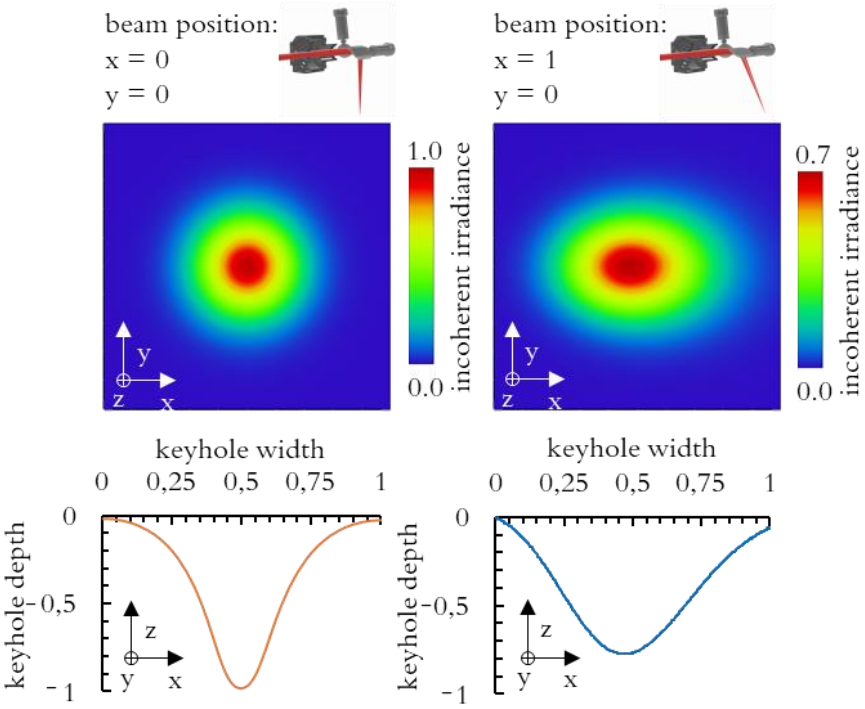

***Figure 7** - Normalized intensity distribution of the laser focus and resulting normalized dimension of the keyhole (trend illustrated) for the scanner position of the center and for a maximum position of an axis.*

3.5.3 Category II: pre-objective scanning

If the scanner is located between the laser source and the beam focuser, this is referred as pre-objective scanning (PrOS). Here, focusing is enabled by passive

optics. This achieves higher dynamics, is designed for high-power applications and requires no additional control technology.

Similar to PoOS, a single spherical lens results in a spherical focal plane [92]. Therefore, in a planar image field, different spot diameters are present. For this reason, the concept of the flat field scanning lens was developed. Especially in laser material processing, the subclass of the F-Theta lens finds its application [87].

3.5.4 F-Theta focusing lens

The laser deflected by the scanner is focused on a fixed plane over the entire scan angle range. The special feature of the optical design of F-Thetas is that they are designed in such a way that a barrel-shaped image field distortion is generated, which counteracts the pincushion image field distortion of the scanner [87,93]. A complete compensation of the distortion is not possible. The result is a combination of both distortions (figure 8).

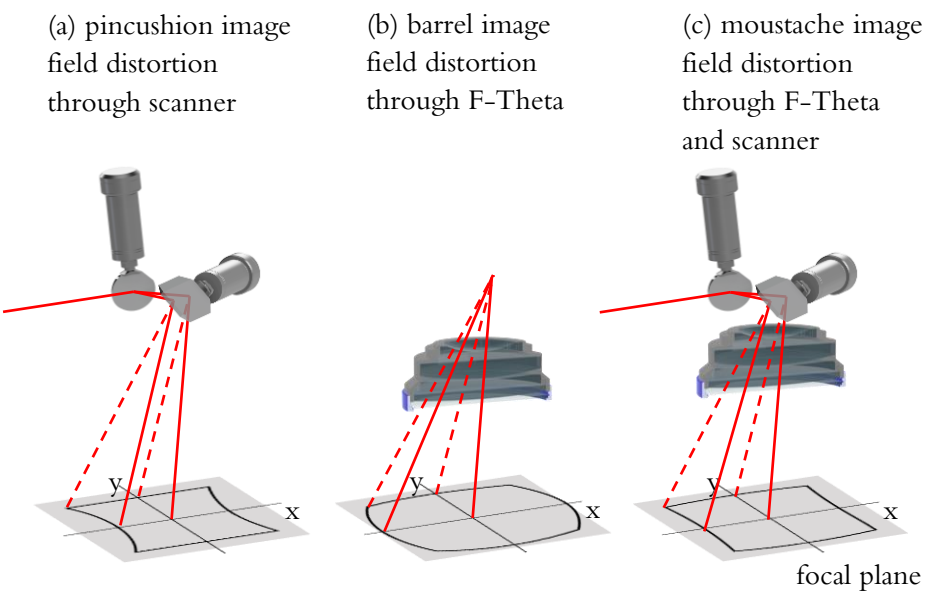

***Figure 8** - Different image field distortions of the components in laser scanner systems*

Since the pincushion image field distortion through the scanner is axisymmetric and that of the F-Theta is point-symmetric due to the spherical lens. The outcome

is a low mustache image field distortion [93,94]. The lenses are optimized to the point where direct proportionality between the field position f and θ with the focal length f is now possible (equation 25). If this is fulfilled, the F-Theta relation is given [95].

$$F(x;y) = 2f \cdot \theta \qquad \text{Equ. 25}$$

In optical design, this condition is typically met to an accuracy of 0.1°. However, this only applies to beams originating from the entrance pupil of the F-Theta. The distance of the entrance pupil A_p is defined as the origin of the deflected laser with the maximum possible beam diameter of the laser. In systems with one scan mirror, the maximum beam diameter can be selected, in contrast to systems with two mirrors. Here, the pupil is placed between mirror 1 and mirror 2, and the distance between pupil and mirrors should be equal and minimal. Consequently, the diameter of the laser increases due to the deflection of the mirrors and the resulting broadening of the beam at the origin of the center of rotation. The entrance pupil diameter A_D necessary for the design results from the entrance beam diameter D_{EB}, the deviation of the ideal position of the entrance pupil L and the maximum deflection angle of θ_{max} according to equation 26. A graphical overview of some parameters is given in figure 9.

$$A_D = D_{EB}\left[1 - \left(\frac{2L}{D_{EB}}\tan\theta_{max}\right)\right] \qquad \text{Equ. 26}$$

$$A_p = \frac{d_1}{2} + d_2 \qquad \text{Equ. 27}$$

Using θ_{max} together with the focal length f, the diameter of the scan field D_F can be calculated (equation 28).

$$D_F = 2\,f \cdot \theta_{max} \qquad \text{Equ. 28}$$

In this respect, a larger focal length enables a larger scan field. In turn a larger focus diameter D_S appears. The focal diameter also depends on the focal length used and the input beam diameter D_{EB}. Depending on the beam source and the definition of the spot, an aposidation factor ζ must also be taken into account, which describes the clipping of the beam [12]. For a Gaussian input beam which is truncated at a D_{EB} = 1/e², the factor is ζ = 1.83. For an input beam with the same intensity distribution over D_{EB}, a so called "tophat", D_S can be estimated with ζ = 2.44. These estimates would only be valid for diffraction limited optics with an angle of incidence σ possible for the F-Theta and scanner (equation 29).

$$D_S = \left(\zeta \cdot \lambda \cdot \frac{f}{D_{EB}}\right)/\cos(\sigma) \qquad \text{Equ. 29}$$

σ depends on the position of the focus in the working area. Consequently, the spot size is not constant over the working field even with F-Thetas. Furthermore, the moustache image field distortion through F-Theta and scanner also influences D_S. An accurate prediction of the spot size in the field can be made by optical simulations. Figure 10 shows a typical simulation plot of the spot size variance for an F-Theta. Similar to the PoOS systems, σ causes an ellipticity of the spot, with symmetry in direction of the field. However, much smaller angles occur here, leading to a lower ellipticity.

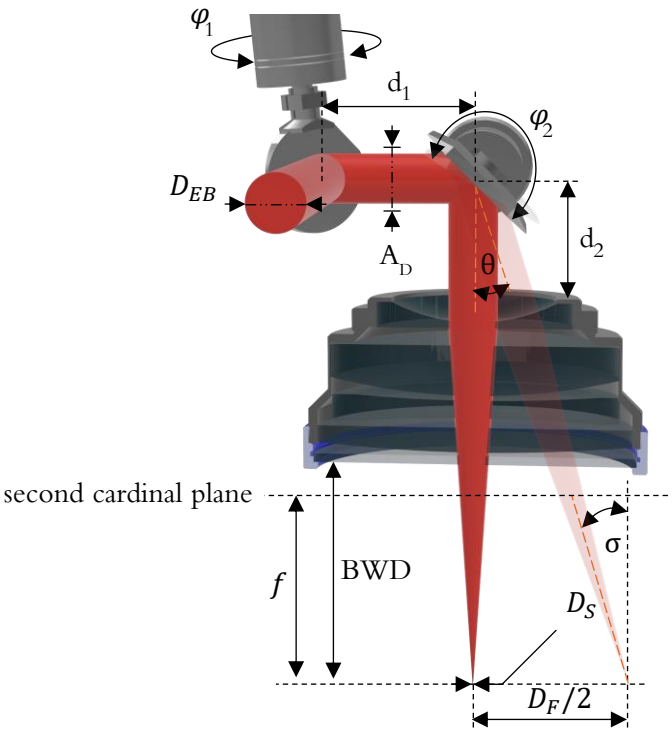

***Figure 9** - Schematic illustration of the sizes and parameters for F-Thetas*

There are special F-Thetas where $\sigma_{(x,y)} = 0°$ for all working area positions, they are called telecentric F-Thetas [93]. The telecentric quality of normal F-Thetas is given by the telecentric angle, which is the maximum angle of incidence σ of the paraxial beam of the output beam [96]. Figure 11 c shows an exemplary design of a telecentric F-Theta. This special form of F-Thetas is characterized by its homogeneous processing of the working field by the identical

AOI. Because $\sigma_{(x,y)} = 0°$ for paraxial beams, the individual lenses must have at least one diameter of the working field D_F. Therefore, due to the cost-benefit factor, only smaller working fields are covered with such lenses. Similar to optical distortion, due to different symmetries of a two mirror scanner and the F-Theta $\sigma_{(x,y)} \neq 0°$. A telecentricity error (typically $\sigma_{max} < 1.5$ °) occurs, because no mirror is on the entrance pupil in a two mirror system.

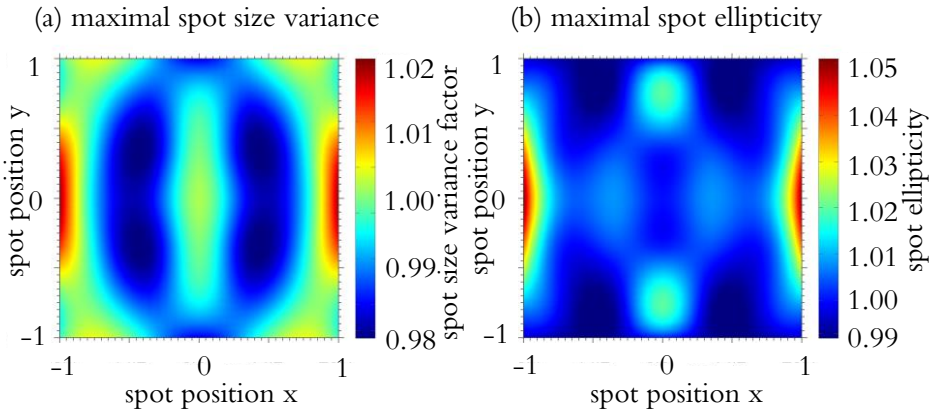

***Figure 10** - Optical simulation of (a) the factor for the spot size variance and (b) the ellipticity in the working field with an F-Theta. The ellipticity describes the fraction of the ellipse axis in direction of the field and perpendicular to it. The position 1 describes the maximum possible field position and angle of incidence.*

With larger input beams, a smaller focus is possible. The maximum possible D_{EB} and the focal length f are the adjusting screws [97] for the estimation of possible applications with PrOS optics. Compared to simple lenses, the focal length of F-Thetas does not describe the real working distance. The optical effect of the complete F-Theta is thereby summarized on an ideal thin lens. The focal length expresses the theoretical distance between the second cardinal plane of the ideal thin lens and its paraxial focus point. The working distance for F-Thetas is expressed by the back working distance (BWD) and describes the free distance between the last optical surface and the focal plane. In optical design, F-Thetas are made possible by a combination of meniscus, plano-concave, plano-convex, biaplanatic, concentric and confocal-aplanatic lenses [87,96]. The tuning among them is achieved by selecting optical lenses with different refractive indices and defined air spacings between the lenses. A characteristic design can be found in figure 11 b. Preferably, the first lens is designed as a plano-concave and the following two as plano-convex. In the simplest case, the surfaces curvature $C_2, C_3, C_5 \approx 0$ are kept for this purpose. In this case, the plano-convex lenses

can be made from the same optical glasses. Typically, a combination of crown and heavy flint lenses is used because the large difference in refractive index allows a compact design and less material [96].

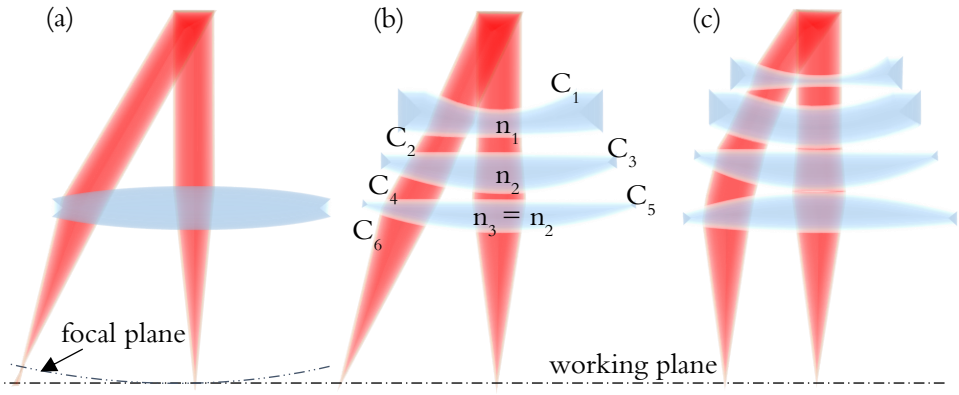

***Figure 11** - Comparison of different PrOS focusers based on their exemplary lens design (a) simple spherical lens, (b) F-Theta and (c) telecentric F-Theta*

For time-intensive applications with laser powers above 150 W, lenses made of fused silica are preferably used because of the lower material absorption [98]. Otherwise, the absorption causes the glass to heat up and the associated change in the refractive index leads to a so-called thermal focus shift [23]. Due to the poor thermal conductivity of the glasses, this phenomenon occurs very locally and mostly in the shape of the scan pattern [23,99,100]. At these locations the BWD will differ after some processing time and the result of the processing will look quite different. The degree of defocusing Δz can be calculated via equations 30 and 31 [100]. A distinction must be made between tophat (equation 30) and Gaussian (equation 31) intensity distributions of the input beam. The laser power P, the focal length f, the thermal derivative dn_i/dT_t of the refractive index n, thermal expansion coefficient α, the heat conduction coefficient γ, the beam diameter D, and the absorption coefficients for the coating Ψ and the glass Ω with thickness d. The index i represents the individual lens in the system.

$$\Delta z_T = -P \cdot f^2 \sum_i \left(\frac{dn_i}{dT_t} + (n_i - 1)\alpha_i\right)\left(\frac{2\Psi_i + \Omega_i d_i}{\pi\gamma_i}\right)\left(\frac{2}{\pi D_i^2}\right) \quad \text{Equ. 30}$$

$$\Delta z_G = \ln(4)\Delta z_T \quad \text{Equ. 31}$$

Even though fused silica has a high thermal expansion coefficient compared to crown glasses, they are more suitable for the use of thermally stable lenses due to

their lower absorption [101,102]. A comparison of typical optical glasses is shown in table 2. Another application of fused silica systems is found in ultra-short pulse (USP) laser material processing. Due to the low electron density of fused silica, the non-linear interactions of the short pulses in the lens are minimized and a higher laser induced damage threshold (LIDT) is possible [24], which indicates the laser intensity resistance of the lens.

***Table 2** - Overview of optical parameters of typical optical glasses for laser optics. The refractive index for λ = 1070 nm, Abbe number at the standard wavelength of 587 nm, internal transmission subtracting the reflection for a 25 mm thick glass sheet and reflection under normal incidence are shown. [101,102]*

Material	n_{1070}	v_A	T [%]	***R [%]***
N-FK5*	1,4785	70.41	99.8	3,73
N-BK7	1,5066	64.17	99.7	4,09
N-SF11	1,7540	25.68	99.8	7,50
N-SF57	1,8113	23.78	99.7	8,33
N-LAF21	1,7689	47.49	99.6	7,71
N-LASF41	1,8133	43.13	99.5	8,36
FS 7980**	1,4496	67.81	99.9	3,34

* "N" describes a variant of optical glass without lead
** FS stands for Fused Silica

A disadvantage of optics made of only one optical material is the resulting color error [96]. Due to the same materials, no compensation with different dispersions is possible. The dispersion describes the wavelength-dependent refractive index of a material. Two incoming rays of different wavelengths are refracted differently in a glass with a high dispersion and are also focused on different focal planes. This error increases for F-Thetas starting from the center of the working field to the edge. Since a laser emits monochromatic radiation, most F-Thetas are not designed to correct the color error by aromatization or apochromatization. In the case of broadband USP or diode lasers, this leads to blurred imaging and thus to a limitation of the minimum achievable focal diameter. Also, color-corrected lenses pose a major challenge for coaxial process monitoring. Since the monitoring is performed at wavelengths deviating from the laser, the observed zone and the zone processed by the laser do not coincide, especially in the edge areas. The achromatization of such a system can be realized for example by a combination of a convex lens with a high Abbe number and a concave lens with a low Abbe number [103]. However, it must be ensured that the lenses used have sufficient transmission for the wavelengths used. The more lenses are used in a system, the more phase transitions of a passing beam between the optical materials are present. As described in chapter 3.2.3, a phase transition always leads to a

reflection of a certain portion of the radiation. In the exemplary fused silica system shown in figure 11 c, this leads to a reflection-induced power loss of approximately 28 % for a laser with a wavelength of λ = 1070 nm. Therefore, all lenses are provided with an optical coating specially adapted to the wavelength used, to reduce the reflection-induced power losses. Thus, the functionality of almost all optical components is only made possible by optical coatings.

3.5.5 Optical coatings for laser optics

Optical coatings are thin-film technologies, which usually have a thickness in the order of magnitude of the light wavelength used [104]. The coatings are typically applied to the lenses by physical or chemical vapor deposition. The effect of optical coatings is based on interference effects and the intrinsic properties of the coating materials. With a suitable coating selection, the reflection, absorption, polarization, phase and transmission can be specifically adjusted. Mirror and anti-reflection coatings can be based on the refractive index difference between the optically active surface and the medium adjacent to it via the resulting effect of constructive and destructive interference. Anti-reflective, mirror and polarization coatings can be realized. Anti-reflective coatings are used in transmissive beam shapers such as laser collimators, optical z-axes or F-Thetas. Mirror coatings are used for beam deflectors, such as the galvo mirrors for the scanning systems.

In the following sections, the three most important coatings for laser material processing are described.

3.5.5.1 Anti-reflective coating

Anti-reflection (AR) coatings are used to achieve the best possible coupling of light during a material transition. Therefore, the refractive index of the coating n_{AR} must lie between the refractive index of the adjacent medium n_m and the substrate n_s. The situation can be determined more precisely using Fresnel's formulas[32,33]. However, a simple estimation can also be carried out via the quadratic mean:

$$n_{AR} = \sqrt{n_m \cdot n_s} \qquad \text{Equ. 32}$$

To achieve an even better anti-reflective effect, several layers can be applied. That can create a refractive index gradient between the boundary medium and substrate or destructive interference effects [105]. The anti-reflection effect is strongly dependent on wavelength and angle of incidence, and adapted coatings are available for separate wavelengths or spectra. This results in different systems like single layer AR with a low refractive index layer, narrow band AR with a V-reflection coating consisting of two layers or broad band AR which consist of more than two different layers and materials [105–108]. The V-reflection coating is named after the characteristic V-shaped reflection curve, which provides good anti-reflection performance only in a small range of wavelengths (see figure 12). Such coatings are preferably used for laser optics which are optimized for the laser wavelength. The disadvantage would be that in other wavelength ranges a higher reflection than the base material is caused. For a larger anti-reflection range, broadband coating systems consisting of several individual layers are used. However, due to surface effects, defects at the layer transitions and intrinsic absorption of the materials, high anti-reflection effects cannot be achieved for discrete wavelengths. Also, the coating procedure is more complex and costly. However, such coating systems are mandatory for optics through which process monitoring at multiple wavelengths are also to be performed.

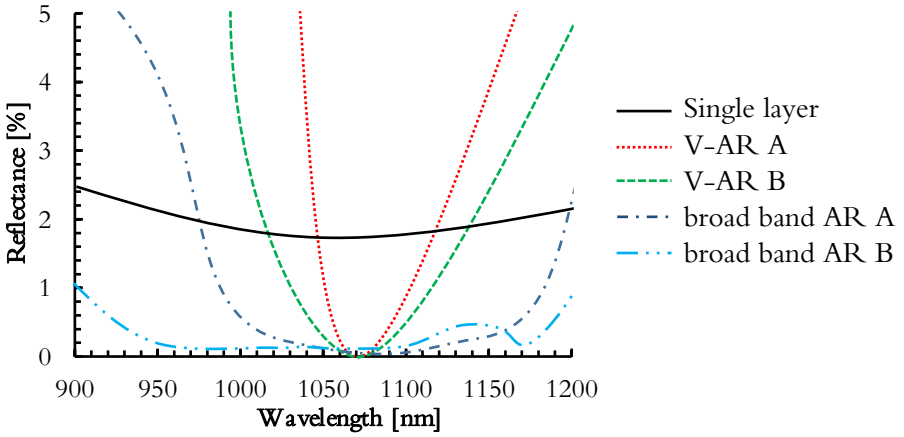

***Figure 12** - Exemplary of the dependence of the reflection on the wavelength for different anti-reflection coatings at λ = 1070 nm for a fused silica-air system at AOI = 0°.*

Usually, oxide or fluoride coating materials [109–117] (see table 3) are used and selected according to the application or substrate material [104–108,118,119].

Oxide coatings are very hard and are only slightly susceptible to contamination due to the high packing density of the coating on surrounding media. Due to

their resistance, oxide layer systems are used for optical components that are in direct contact with the process atmosphere in LBPF systems.

Fluoride coatings, on the other hand, are very soft due to their low packing density and are also partially water-soluble. Therefore, these coatings are susceptible to contamination. In general, however, a better anti-reflection effect can be achieved with a fluoride-based AR coating [118]. Therefore, in many optical systems, the fluoride coatings are applied only to internal interfaces in the system. The lens surfaces, which are exposed to external influences, are coated with oxides.

***Table 3** - Overview of coating materials with achievable refractive index for λ = 1070 nm [109–117]*

Coating class	Effect	Material	n_{1070}
fluoride coatings	high refractive	LaF_3	1.6007
	low refractive	MgF_2	1.3761
		$LiCaAlF_6$	1.3865
		CaF_2	1.4284
oxidic coatings	high refractive	Al_2O_3	1.7654
		HfO_3	1.8809
		Y_2O_3	1.9009
		Sc_2O_3	1.9872
	low refractive	SiO_2	1.4496

Another possibility of anti-reflection coating is the structuring of the surface [120]. Here, the so-called "moth eye effect" is used. In this process, the surface of the substrate is structured via a selective plasma etching, photo lithographic or also via electron beam lithography in the order of magnitude up to $\lambda/5$. The structure is used to create a gradual transition between n_m and n_s. The advantage is that such anti-reflection structures are largely angle of incident and also wavelength independent in a wide range. However, such an anti-reflection coating is currently not economically applicable for standard laser optics.

3.5.5.2 High-reflective coating

High-reflective coatings or also known as mirror coatings are intended to do the opposite of AR coating and achieve the highest possible reflection of a spectrum with a very low absorbance [104,105,107]. This is realized via the phenomenon of total reflection. Total reflection can occur during the transition of

electromagnetic waves from an optically denser to an optically thinner medium and depends on the refractive index as well as the wavelength [105,121]. For example, metals are well suited as optical mirror materials due to their dominant imaginary refractive index. In addition, due to the atomic structure with the free-moving electrons, the light ultraviolet to infrared (UV-IR) can penetrate only a few nanometers. The free electrons interact with the incident electromagnetic radiation and emit it back almost completely. Thus, very thin layers are sufficient to achieve the desired mirror effect over a very broad spectrum. Aluminum, silver, copper, gold and chromium have become established as coating materials [122]. However, due to the described interaction, a portion of the incident light is also absorbed. For higher laser powers, a dielectric HR coating must therefore be used [123].

Similarly, mirrors can be created by quarter-wave plate layers [124] with the materials from table 3. The layer thickness d_s of the individual layer can be derived from the relationship in equation 33. Here, n corresponds to the refractive index at the wavelength λ to be mirrored.

$$n \cdot d_s = \lambda/4 \qquad \text{Equ. 33}$$

The individual layers must be alternately high and low refractive and stacked in sufficient numbers to produce destructive interference. The resulting reflection band is specifically adapted to a certain wavelength range and can be transparent to other frequencies. In order to compensate material fluctuations, the thickness

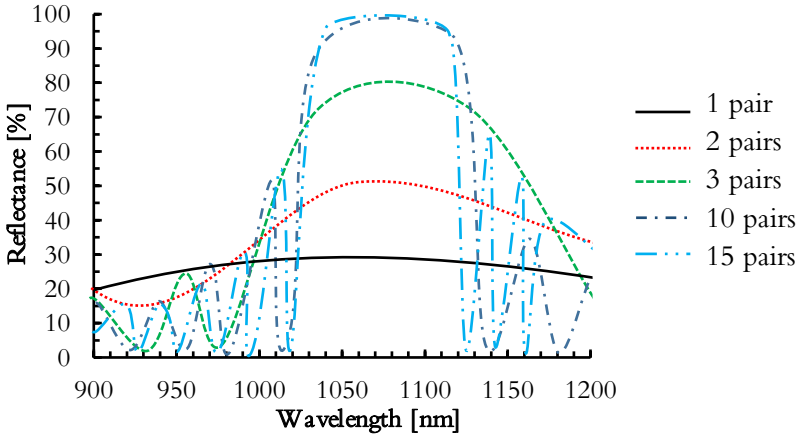

***Figure 13** - Exemplary of the dependence of the reflection on the wavelength for different pair number of a high-reflection coating for λ = 1070 nm for a fused silica-air system at AOI = 45°.*

of the individual layers is optimized during the production of the coatings to the spectral region where a high reflection is to be achieved [125]. Therefore, the position and strength of the remaining peaks in the reflection spectrum cannot be predicted exactly and differs depending on the coating batch. The number of layers required for high reflectance and the spectral width of the reflection band depend on the refractive index difference of high- and low-reflectance layers. For HR-coatings, between 15 to 20 layer pairs are required [121,123,124]. Figure 13 shows an exemplary reflection profile of different numbers of layer stacks.

3.5.5.3 Dichroic coating

Dichroic coatings are a combination of HR and AR coatings [126]. The coating design for a certain spectral range is designed to produce destructive interference. A corresponding highly reflective effect is achieved. For another part of the spectrum, the coating design produces a specific constructive effect, which allows an anti-reflection behavior for the spectral range. Thus, a part of the spectrum is reflected by the layer and the other part passes through with minimal losses. An exemplary spectrum of a dichroic mirror is shown in figure 14.

These coatings find their application as divider cubes for coaxial process monitoring [127,128]. Different spectral paths can be superimposed, such as the laser with an imaging channel on a shorter wavelength [129]. It can also be used

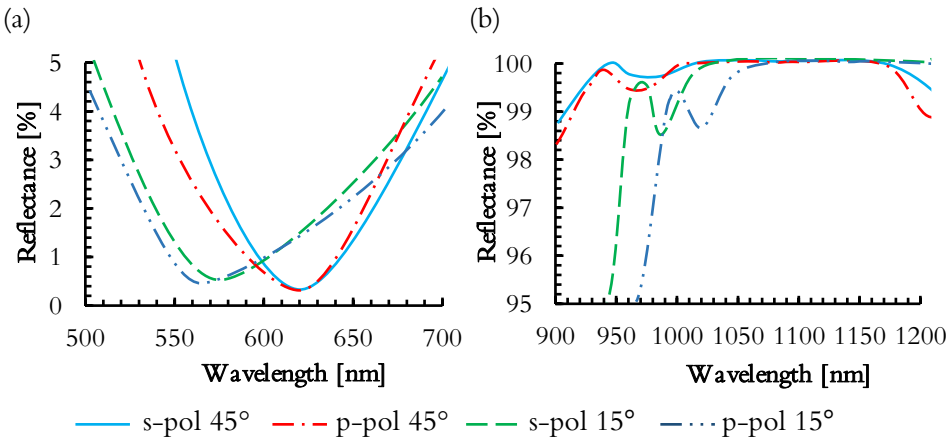

***Figure 14** - Example of the reflectance spectrum of a dichroic coating for two different angles of incidence and for s- and p-polarized light. In (a) the anti-reflection spectral range for λ = 620 nm and in (b) the highly reflective range for λ = 1070 nm are shown.*

as a separator to split a spectral signal and evaluate the individual spectral components, such as in a two-color pyrometer. In the application, the spectral component with the higher power is usually reflected and the one with the lower power is allowed to pass, since the HR effect has a lower power loss.

In contrast to the dielectric AR and HR coatings, dichroic coatings are even more dependent on the AOI and on the polarization of the radiation. Since there are interference effects for two areas, the reflectance spectrum is influenced differently by the AOI depending on the design [126]. One of the reasons for this is that the path of the paraxial beam is geometrically longer in the layer stack at larger angles of incidence compared to the path of a beam that hits the layer at normal incidence. Thus, the individual layer thicknesses d_s varies depending on the AOI. That causes different interference effects. The shorter spectral range reacts more sensitively to a d_s deviating from the nominal one due to the shorter wavelengths and the condition from equation 33 is no longer fulfilled.

In process monitoring for example, measurement signals of different strengths for varying angles produced. In order to keep the incidence angle influence as low as possible, the maximum permissible AOI is an important design criterion for dielectric coatings. The layer design of a dichroic mirror is therefore very complex and can comprise up to 100 layers.

4 Methodological approach

The spectral behavior and the interaction with electromagnetic radiation of powders for additive manufacturing were investigated in the three papers using several tools and analysis methods. Figure 15 shows the spectrometric techniques central for the papers. Other methods were also used to verify the results, which are briefly explained in the following chapters.

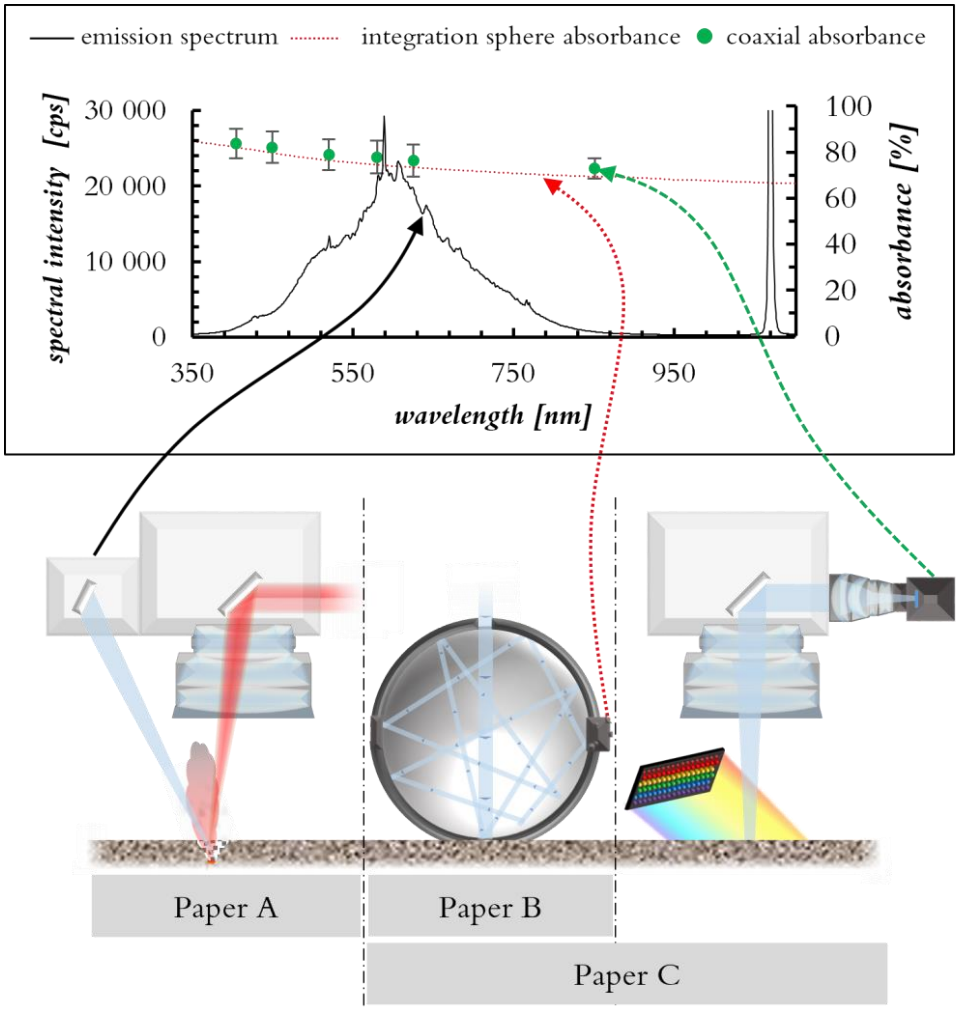

***Figure 15** - Overview of spectral measurement methods of powders for additive manufacturing. The upper part shows the measurements from the three papers for the same Inconel 718 sample.*

4.1 Optical spectroscopy

A spectrometer can be used to separate the spectral components of light and measure the intensity distribution of the individual components [130]. In principle, there are two different types of optical spectrometers [131]. On the one hand there are spectrometers which have their own calibrated light source with monochromatic radiation and detect the backscattered or transmitted components of their own light source. Here, portions of light after passing through a medium can be analyzed in relation to the absorption within the medium. In paper B and C the absorbance of the investigated powders was measured via the backscattered spectrum.

On the other hand, there are systems where external light is introduced and which display the intensities of the irradiated wavelengths. In the latter case, only relative spectra can be acquired without a calibrated emitter. In paper A, the spectrum of laser material interaction at different angles was observed via such a spectrometer

In both cases, the decomposition of the light or the monochromatization is technically realized by a diffraction grating or prism [131]. By using a diffraction grating instead of a prism for spectral decomposition, the spectral resolving capability can be improved and a more compact design of the system can be achieved. To increase the resolving capability, multiple prisms and diffraction gratings can be connected in a row. The spectral resolving capability AV is defined by distance the single wavelengths $\Delta\lambda$ can be separated (equation 34).

$$AV = \lambda/\Delta\lambda \qquad \text{Equ. 34}$$

The light is collimated onto the elements within the spectrometer using concave mirrors, as no color errors are introduced by reflective elements. The intensity can be detected by photodiodes or image sensors like CMOS sensor.

Optical spectrometers are the tool of choice for making highly accurate statements about the transmission, reflection and absorption properties of materials. They can also be used to measure the emission behavior of materials [132]. A common form in laser technology is laser induced breakdown spectroscopy (LIBS) [133]. In LIBS, a pulsed laser system is used in combination with a spectroscopic measurement channel. The laser is focused on a target and the high intensity vaporizes the material and creates a high temperature plasma. Part of the emitted spectrum of excited atoms and ions is collected and spectrally analyzed [134]. By knowing the characteristic atomic transitions, conclusions can be drawn about both the qualitative and quantitative composition of the target [135]. Similar

principle can be applied to the spectral analysis of the process zone during deep penetration welding (paper A).

4.2 High speed imaging

High speed imaging is a tool used only in paper A. In this process, a large number of images are captured in a very short time. Typical orders of magnitude are 15 000 to 50 000 images per second [136]. Viewed individually or stitched together as a video, phenomena and interactions can be studied in the µs range. Due to the large amount of data, it is important to have good synchronization (triggering) of the recording to the investigated events. In paper A, the expansion of plasma and metal vapor during deep welding was investigated from the HSI images. For this purpose, a filter was placed in front of the HSI camera, which only blocks the laser wavelength and only the plasma emission or metal vapor emission is visible in the images. In the post-processing of the data, the propagation direction, velocities of particles whirled up, the oscillation of the plasma and the spectral intensity could be derived. Such information cannot be obtained from a single timed image. In another aspect of paper A, superimposed images were generated from the individual frames of the images. The pixel data from 131 single shots were added together. Particularly bright pixels indicate a place where the plasma or the metal vapor was most concentrated during the exposure.

4.3 Digital imaging techniques

Imaging techniques cover a very wide range. The key point is the acquisition of a two-dimensional data set, which represents the geometric properties of the object to be examined. The pixels of the digital image data are set in relation to a metric size. This allows the derivation of real structure and object dimensions. Such a method is advantageous in connection with a magnified image of the object to be examined. The simplest method is light microscopy, in which an illuminated object is imaged onto a sensor via an optical lens system. In paper B, light microscopy was used to analyze the shape of particles of some powders. The maximum resolving capability AD of objects can be determined by the Abbe limit [137]. Here β is half the aperture angle of the objective. The product of the refractive index and the sine of half the aperture angle is the numerical aperture of the used optics (equation 35).

$$AD = \frac{\lambda}{\mathrm{n} \cdot \sin\beta} \qquad \text{Equ. 35}$$

However, for smaller structures and larger magnifications, light microscopes are limited by their shallow depth of field [138]. Electron scanning microscopes offer an alternative [139]. Here, a resolution down to single-digit nanometers is possible [139]. Due to the scanning signal acquisition over the 2-dimensional plane, an increased depth of field is also given. As a result, even surface image can be captured. In papers B and C, electron scanning microscope images of the powders were made to validate grain size and spherical particle shape.

In paper A and C, a not very common method of surface imaging was used. Here, images of the process surface were taken coaxially through the laser material processing optics. Depending on the F-Theta used, an AD = 5 - 20 µm is possible. The setup of this system is described in detail in papers A and C. In paper A, a single image was taken at certain scanner positions, where the process zone was evaluated in the image section. A statement on the width of the melt zone and the generated spatter was possible, which was linked to the HSI images. With the setup and methodology developed in paper C, it is possible to image the entire process area of 114 mm x 114 mm with the described resolving capability of AD = 5 - 20 µm. Similar to the electron scanning microscope, the surface is scanned and stitched into one image. The advantage of such surface imaging is that it can be performed in-situ in the system and no external analysis step is necessary.

4.4 Grain size determination

In order to investigate the relationship between absorbance and grain size diameter in paper B and C, an exact grain size distribution had to be determined for all powders. A fundamental tool is the grain size analysis. A very simple method describes the sieving of the powder with sieves of different mesh sizes distance [140]. The fraction passing through the sieve and the fraction retained are weighed and related. Technically, it is realized by several sieves with decreasing mesh size distance. The particle analysis based on laser diffraction is more accurate and easier to perform [140]. Here, the principle of Mie scattering at spherical particles is used, which means that large particles have a small deflection angle in relation to the wavelength and small particles have a large deflection angle [141,142]. The powder is inserted into a laser beam path in a controlled manner and the scattering pattern of the laser is monitored. Then the

size of the particles can be calculated. It is important that the particle size is approximately in the order of magnitude of the used wavelength. This procedure was performed for paper B and C and validated using the light and electron scanning microscope images. A statistical particle size can also be derived from surface images.

4.5 Optical simulation

Optical simulations are a theoretical tool. They require a detailed model of the optical system, which includes all optical elements and their exact optical behavior. It contains the exact refractive indices, transmission values, distances between the elements and the exact geometric shape of the elements. Ray geometry correlations can be made, allowing the path of a single ray from the object through each element of the system to the image plane to be calculated. This is known as a sequential method. It allows the behavior of the entire optical

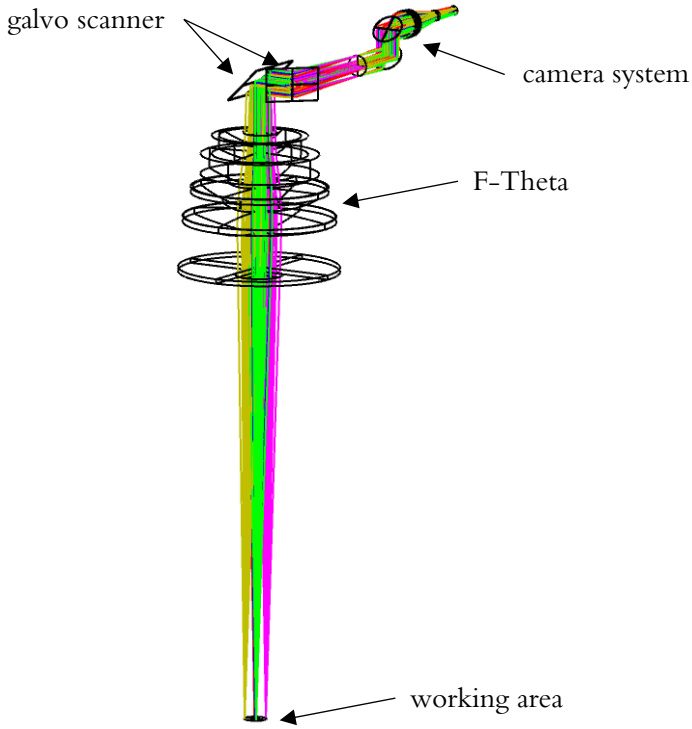

***Figure 16** - Zemax 3D layout of the sequential model of the optical system used for the calculation of the camera correction for paper C*

system to be predicted and provides a basis for selecting suitable optical components for a real system. One of the most popular simulation programs is Zemax, which was also used for this thesis.

In paper A the alignment and control of the reflective monitoring system was calculated and the laser parameters on the workpiece were simulated. A comparison with the simulated data and the measured data can be used to eliminate measurement errors or to improve the model. In paper C, the optical image of the camera was calculated for the different wavelengths in order to create a correction of the image field distortions for each position in the scan field. Figure 16 shows the optical sequential model of the system used in paper C as an example.

Another possibility of an optical simulation is ray tracing, which is known as a non-sequential variant. Here, a ray is emitted from a defined source and traced until it hits a defined detector area. In contrast to the sequential method, optical surfaces can be hit multiple times. This simulation variant is very computationally intensive since it is based on the trial-and-error principle. It is used for the calculation of scattered radiation in lenses or for the simulation of the optical behavior of real surfaces, such as powders. In papers B, ray tracing was used to estimate the measurement error of the integration sphere, and in paper C, to estimate the backscattering ability of a powder surface.

5 Summary of the papers

Paper A: Angular dependence of coaxial and quasi-coaxial monitoring systems for process radiation analysis in laser materials processing

Abstract: Process monitoring is becoming increasingly important in laser-based manufacturing and is of particular importance in the field of additive manufacturing [e.g. Laser Powder Bed Fusion (LPBF)]. Process monitoring enables a reduction of production costs and a lower time-to-market. Furthermore, the data can be used to create a digital twin of the workpiece. There are already many established processing head-integrated monitoring systems for such applications as the multispectral analysis of process radiation. However, the monitoring of complex signals in systems with F-Theta scanner lenses is very challenging and requires specially adapted optics or measuring sensors. In this paper a potential arrangement for spectroscopy-based process monitoring in pre-objective scanning is presented. The process radiation was monitored using a coaxial and a quasi-coaxial observation system. The measurements were carried out on both a solid and a powder coated sample of 2.4668 (Inconel 718) to show the potential use of these systems in laser-based additive manufacturing. In order to obtain comprehensive data about the process signal, the process zone was analysed at different angles of incidence (AOI) of the laser using a high-speed camera (HSI) and a spectrometer. The connection between the HSI and the spectral measurements is discussed. The ionization of the material and the formation of a plasma was observed and found to lose intensity as the angle of incidence increases. A model of the system that demonstrates the intensity of the emitted radiation of the plasma was created. It enables the measured values to be corrected. The corrected measurement data can be used to detect impurities or a non-ideal energy input across the entire processing field, which is a move towards robust process monitoring.

***Conclusions*:** The shape of the process signal for scanning laser material processing using an F-Theta lens was examined. The shape is dependent on the angle of incidence. For this work a coaxial and a quasi-coaxial measurement setup were built with which the spectral signal of the process radiation was analysed.

- With the coaxial setup, the short-wave components of the spectrum (below $\lambda < 510$ nm) cannot be detected even at a scanner mirror angle of 5 ° due to the chromatic aberration of the F-Theta lens.

- With the reflective quasi-coaxial set up, the process signal could be accurately recorded.
- A spectral signal of the process radiation over the entire processing field could be measured via both setups.
- When using typical LPBF parameters, discrete peaks at $\lambda = 426$ nm and $\lambda = 520$ nm in the process radiation can be observed by spectroscopy. These peaks can be attributed to the chromium in the stainless-steel sample material.
- As the angle of incidence of the laser to the workpiece increases, the measured spectral intensity decreases. From the centre of the scan field to the last measuring point in the working area of the F-Theta lens, the spectral intensity decreases without correction by 36 % for solid samples. This is associated with variations in spot size and the interaction zone as a function of the angle of incidence.
- The powder coated sample has a greater decrease (of 51 %) in spectral intensity with increasing angles of incidence compared with the solid material.
- The measured spectral intensity distribution for solid materials can be adjusted over the entire field by means of a correction factor. This correction includes a function that describes the numerical aperture of the measuring channel and the laser intensity on the working field.
- Any remaining deviation in the corrected field measurements can be traced back to the geometry of the setup and the field-dependent angle of the process radiation.

Paper B: Absorbance study of powder conditions for laser additive manufacturing

Abstract: Absorbance is often used for simulations or validation of process parameters for powder-based laser materials processing. In this work, the absorbance of 39 different metal powders for additive manufacturing is determined at 20 different laser wavelengths. Different grain sizes and aging states for: steels, aluminum alloys, titanium alloys, Nitinol, high entropy alloy, chromium, copper, brass and iron ore were analysed. For this purpose, the absorbance spectrum of the powders was determined via an UV-VIS-NIR dual-beam spectrometer in the range of λ = 330 - 1560 nm. At the laser wavelengths of λ = 450 nm, 633 nm and 650 nm, the absorbance averaged overall materials was found to increase by a factor of three compared to the usual wavelength of λ = 1070 nm, with minimal variations in absorbance between materials. In the investigation of the aged or used powders, a loss of absorbance was detectable. Almost no changes from the point of view of processing aged and new AlSi10Mgpowders, is expected for laser sources with λ = 450 nm. The resulting measurements provide a good basis for process parameters for a variety of laser wavelengths and materials, as well as a data set for improved absorbance simulations.

Conclusions:

- Several absorbance values determined in the literature using ray tracing were confirmed experimentally on powder beds. In addition, other absorbance values of 1.4404, 2.4668, AlSi10Mg and Ti64 powders for
- λ = 1070 nm measured experimentally in the literature were also confirmed.
- When using a laser source with λ = 450 nm (SDα = 4.8), λ = 635 nm (SDα = 2.3) or λ = 650 nm (SDα = 2.6) for a laser powder bed fusion process, the absorbance deviation SDα between the investigated materials is lower and the coupling efficiency is 2.4 up to 3.3 times higher than the commonly used laser source with λ = 1070 nm
- (SDα = 10.6).
- The smallest absorbance deviation between the aged and virgin AlSi10Mg powders is at a laser wavelength of
- λ = 450 nm, which allows the same processability regarding the coupling efficiency.

- A mean increase in the absorbance spectrum of absolute 6 % was proven for smaller grain size fraction for 1.4404 and 2.4 % for 1.4542 compared to larger grain size fractions of the same material.
- With increasing absorption due to shorter wavelengths, the influence of grain size on absorbance becomes smaller.
- For all used, oxidized or specifically aged powders, a loss of absorbance in the VIS-NIR range and an increase in absorbance in the UV range can be observed. The change in the spectrum can be traced back to oxide layers on the particles and could be shown in the case of 1.4404 and 1.2344 on the theoretically calculated absorption spectra of Fe2O3. The same applies to AlSi10Mg and the absorption spectrum of Al2O3.
- For 46 h and 96 h aged AlSi10Mg powders, only a maximal difference between the spectra of 0.7 % is measurable, resulting in spectral indistinguishability between the age states between $\lambda = 330 – 1560$ nm.

Paper C: Proof-of-concept of an absorbance determination of a powder bed by high resolution coaxial multispectral imaging in laser material processing

Abstract: Imaging techniques are very popular for process monitoring in laser material processing due to their high information content. At the same time, coaxial systems focused by passive laser optics still present a major challenge. Since most laser optics cause imaging errors for the monitoring channel. In this paper, the design, methodology and procedure is shown to be able to acquire coaxial image data by standard laser components. This is shown by components for a laser powder bed fusion system and their use on a powder bed. The focus is on the correction of the image data to produce a high-resolution, geometrically correct and gap-free overview image of the entire processing plane. For this purpose, optical simulations of the system are performed to detect aberrations, distortions and chromatic errors and to correct them by hardware elements or in software post-processing. Over the entire 114 mm x 114 mm working field, objects can be captured geometrically correctly with a maximum deviation of 22 µm - 49 µm, depending on the wavelength. By capturing images at wavelengths of 405 nm, 450 nm, 520 nm, 580 nm, 625 nm and 850 nm, multispectral information is gained over the entire working plane. In addition, an absorbance of the powder bed is derived from the images. To qualify this methodology, tests are performed on 20 different powders. These include different particle sizes, aged and oxidized powders of different metals. The ability to determine absorbance is simulated by ray tracing powder surfaces. This allows the determination of in-line absorbances from the powder bed with a maximum deviation of 2.5 % compared to absorbance spectra of established methods. This allows the origins of component defects such as foreign particles, powder oxidation, spatter and uncoated areas to be identified down to a diameter of 20 µm.

Conclusions: Blown powder directed energy deposition was successfully carried out with the process described and observed through high-speed imaging. Due to the highly focussed powder stream and laser beam configuration, an island of unmelted powder formed in the melt pool (at the centre of the laser spot). Some of the powder grains ricochet off the island, resulting in decreased catchment efficiency.

- The proof-of-concept of an absorbance determination of a powder bed by high resolution coaxial multispectral imaging in laser material

processing has been performed on 20 different powders and the applicability has been demonstrated.

- Coaxial multispectral imaging of the entire processing field through the laser optics is possible in six wavelengths (UV-IR) and objects can be imaged geometrically correct with a maximum error of 49 µm.
- From the histograms of the recorded images, a grayscale value can be formed for each wavelength, from which the absorbance of the material in the working plane can be derived. The maximum error was an absorbance difference of $\Delta\alpha$ = 8.4 % to a value determined with a conventional spectrometer method. If the materials and the absorption behavior are known, a maximum deviation of $\Delta\alpha$ = 2.5 % can be achieved by optimization
- In combination with the derived absorbance and the high-resolution stitched overview image, a multispectral overview image can be formed, which allows a material differentiation.
- Foreign particles, powder oxidation, spatter and uncoated areas up to a diameter of 20 µm can be detected on the entire working area and geometrically correctly located.
- Due to the light scattering behavior, the particle geometry of the powder has a direct influence on the determined absorbance value, which leads to incorrectly derived absorbance in the case of large particle diameter deviations ($\Delta D > 40$ µm).
- A slightly defocused image can be used to derive a more accurate absorbance, since the variance of the grayscale value distribution is reduced by non-imaged contours and direct reflections of the illumination.

6 General conclusions of the thesis

This thesis deals with the basic design of new monitoring techniques and their experimental investigation of the concepts. The focus is on the evaluation of spectral signals. Spectral monitoring of the process or the feedstock provides a lot of information that can be used to determine if the process will be affected by potential defects or if defects have already occurred in the process. Furthermore, the recorded data allow to react in-situ to process changes or provide the basis for the development of new processes. From a scientific point of view, the general conclusions of the work are the following:

- The angular orientation of the measuring beam to the plane of the laser material interaction has the greatest influence on the measured spectrum during the detection of the spectral emission and does not behave linearly over the working field. With increasing angle of incidence, the measured spectral intensity decreases. The same applies to the angle of incidence of the laser at a constant monitoring angle. This influence can be minimized by a correction model (paper B).

- A broad database of absorbance spectra in the range λ = 330 - 1560 nm has been created, containing 16 materials used in additive manufacturing in a total of 39 states. The state of the powder, which includes age, grain size and degree of contamination, can be deduced to some extent from the absorbance spectrum. Furthermore, the data allows process development with other laser wavelengths (paper B).

- The use of shorter wavelengths represents a potential improvement of the process. In particular, this applies to possible laser wavelengths of λ = 450 nm. The absorbance deviation between the 39 investigated materials is lower and the coupling efficiency is up to 3.3 times higher than the commonly used laser source with λ = 1070 nm (paper b).

Furthermore, two engineering conclusions can be drawn from this work:

- The functionality of a quasi-coaxial monitoring system could be shown on the basis of the experimental setup, which allows a monitoring of a broad spectrum (λ = 330 nm - 1200 nm) in pre-objective scanning systems free of optical color error and transmission limitations (paper A).

- The applicability of the principle of high resolution coaxial multispectral imaging and the derivation of absorbances could be demonstrated based on 20 powders. Absorbance differences due to impurities, oxidation and wrong process parameters in the powder bed can be geometrically correctly detected in relation to the laser path (paper C).

7 Outlook

Based on the research of this thesis, some future topics are most promising for the long-term goal of making LBPF more sustainable and industrially viable.

- Development of an F-Theta for coaxial spectral monitoring with corrected lateral and longitudinal chromatic aberration for a range of λ = 350 nm - 2000 nm.

- Simulation of the spectral emission of the laser material interaction during the processing of powders for a system described in paper A.

- Integration of quasi-coaxial monitoring and high resolution coaxial multispectral imaging techniques into a real LPBF system, as well as monitoring of a real printing job.

- Verification of the possible more stable process of aged aluminum powders (AlSi10Mg) during processing with a laser source at λ = 450 nm.

- Further development of high-resolution imaging of the scan field and integration of algorithms for image evaluation, so that printed structures can be measured automatically, grain size determination derived and foreign particles detected.

8 References

[1] M. Srivastava, S. Rathee, Additive manufacturing: recent trends, applications and future outlooks, Progress in Additive Manufacturing. (2021). https://doi.org/10.1007/s40964-021-00229-8.

[2] M. Schmidt, M. Merklein, D. Bourell, D. Dimitrov, T. Hausotte, K. Wegener, L. Overmeyer, F. Vollertsen, G.N. Levy, Laser based additive manufacturing in industry and academia, CIRP Annals. 66 (2017) 561–583. https://doi.org/10.1016/J.CIRP.2017.05.011.

[3] I. Campbell, O. Diegel, J. Kowen, N. Mostow, T. Wohlers, Wohlers Report 2021 - Additive Manufacturing and 3D Printing State of the Industry, 2021.

[4] W.E. King, A.T. Anderson, R.M. Ferencz, N.E. Hodge, C. Kamath, S.A. Khairallah, A.M. Rubenchik, Laser powder bed fusion additive manufacturing of metals; physics, computational, and materials challenges, Applied Physics Reviews. 2 (2015) 041304. https://doi.org/10.1063/1.4937809.

[5] T. Purtonen, A. Kalliosaari, A. Salminen, Monitoring and Adaptive Control of Laser Processes, Physics Procedia. 56 (2014) 1218–1231. https://doi.org/10.1016/J.PHPRO.2014.08.038.

[6] R. McCann, M.A. Obeidi, C. Hughes, É. McCarthy, D.S. Egan, R.K. Vijayaraghavan, A.M. Joshi, V. Acinas Garzon, D.P. Dowling, P.J. McNally, D. Brabazon, In-situ sensing, process monitoring and machine control in Laser Powder Bed Fusion: A review, Additive Manufacturing. 45 (2021) 102058. https://doi.org/10.1016/J.ADDMA.2021.102058.

[7] A. Einstein, Zur Quantentheorie der Strahlung, Phys. Z. 18 (1916) 121–128.

[8] A.L. Schawlow, C.H. Townes, Infrared and Optical Masers, Physical Review. 112 (1958) 1940–1949. https://doi.org/10.1103/PhysRev.112.1940.

[9] T.H. Maiman, R.H. Hoskins, I.J. d'Haenens, C.K. Asawa, V. Evtuhov, Stimulated optical emission in fluorescent solids. II. Spectroscopy and stimulated emission in ruby, Physical Review. 123 (1961) 1151.

[10] G. Herziger, Laser Material Processing, in: M. Onorato (Ed.), Gas Flow and Chemical Lasers, Springer New York, Boston, MA, 1984: pp. 55–67. https://doi.org/10.1007/978-1-4615-7067-7_4.

[11] Kannatey-Asibu E, Laser Pumping, in: Principles of Laser Materials Processing, John Wiley & Sons, Ltd, 2009: pp. 63–70. https://doi.org/https://doi.org/10.1002/9780470459300.ch3.

[12] J. Bliedtner, H. Müller, A. Barz, Lasermaterialbearbeitung: Grundlagen – Verfahren – Anwendungen – Beispiele, Carl Hanser Verlag, München 2013. ISBN: 978-3-446-42168-4

[13] H. Lee, J. Lim, M.J. Low, N. Tham, M. Vadakke Matham, Y.-J. Kim, Lasers in additive manufacturing: A review, International Journal of Precision Engineering and Manufacturing-Green Technology. 4 (2017) 307–322. https://doi.org/10.1007/s40684-017-0037-7.

[14] T. Muangpool, S. Pullteap, Reviews on laser cutting technology for industrial applications, in: Proc.SPIE, 2018. https://doi.org/10.1117/12.2300955.

[15] R. Bogue, Lasers in manufacturing: a review of technologies and applications, Assembly Automation. 35 (2015) 161–165. https://doi.org/10.1108/AA-07-2014-066.

[16] M. v Klein, T.E. Furtak, Die Natur des Lichtes, in: M. v Klein, T.E. Furtak (Eds.), Optik (Stuttg), Springer Berlin Heidelberg, Berlin, Heidelberg, 1988: pp. 1–45. https://doi.org/10.1007/978-3-642-73409-0_1.

[17] M.J. Riedl, Single Optical Imaging Elements, SPIE PRESS, 2017. https://doi.org/10.1117/3.2272475.

[18] Kannatey-Asibu E, Beam Delivery, in: Principles of Laser Materials Processing, John Wiley & Sons, Ltd, 2009: pp. 188–227. https://doi.org/https://doi.org/10.1002/9780470459300.ch9.

[19] J.P. Mathieu, Electromagnetic waves, in: Optics, Pergamon, 1975: pp. 31–48. https://doi.org/10.1016/B978-0-08-017157-9.50007-2.

[20] J.C. Maxwell, On physical lines of force, Philosophical Magazine. 90 (2010) 11–23. https://doi.org/10.1080/14786431003659180.

[21] M. v Klein, T.E. Furtak, Geometrische Optik, in: M. v Klein, T.E. Furtak (Eds.), Optik (Stuttg), Springer Berlin Heidelberg, Berlin, Heidelberg, 1988: pp. 99–147. https://doi.org/10.1007/978-3-642-73409-0_3.

[22] D.Y. Smith, Dispersion Theory, Sum Rules, and Their Application to the Analysis of Optical Data, Handbook of Optical Constants of Solids. (1997) 35–68. https://doi.org/10.1016/B978-012544415-6.50006-6.

[23] A. Hess, R. Weber, T. Graf, M. Schäfer, C. Thiel, Reference process for determination of thermal focus shift, 30th International Congress on Applications of Lasers and Electro-Optics, ICALEO 2011. (2011) 729–734.

[24] D. Hülsenberg, A. Harnisch, Alexander Bismarck, Microstructuring Glasses Using Lasers, in: D. Hülsenberg, A. Harnisch, A. Bismarck (Eds.), Microstructuring of Glasses, Springer Berlin Heidelberg, Berlin, Heidelberg, 2008: pp. 175–196. https://doi.org/10.1007/978-3-540-49888-9_8.

[25] W. Denk, K. Svoboda, Techreview Why Multiphoton Imaging Is More than a Gimmick, Neuron. 18 (1997) 351–357.

[26] N.V. Tkachenko, Two photon absorption, in: Optical Spectroscopy, Elsevier Science, 2006: pp. 293–294. https://doi.org/10.1016/B978-044452126-2/50043-5.

[27] Kannatey-Asibu E, Background on Laser Processing, in: Principles of Laser Materials Processing, John Wiley & Sons, Ltd, 2009: pp. 407–430. https://doi.org/https://doi.org/10.1002/9780470459300.ch14.

[28] F. Dausinger, Strahlwerkzeug Laser: Energiekopplung und Prozesseffektivität, B. G. Teubner Stuttgart, Stuttgart, 1995.

[29] A.M. Prokhorov, Laser heating of metals, A. Hilger, Bristol; Philadelphia, 1990.

[30] A. Salminen, A. Jansson, V. Kujanp, Effect of welding parameters on high-power diode laser welding on thin sheet, Proceedings of SPIE - The International Society for Optical Engineering. (2003) 106–115. https://doi.org/10.1117/12.478366.

[31] L.V.P.R. de Broglie, Recherches sur la théorie des quanta, Annals Phys. 2 (1925) 22–128.

[32] D.G. Smith, Huygens' and Huygens-Fresnel Principles, in: Field Guide to Physical Optics, Society of Photo-Optical Instrumentation Engineers, Washington, 2013. https://doi.org/10.1117/3.883971.ch45.

[33] D.G. Smith, Fresnel Equations, in: Field Guide to Physical Optics, Society of Photo-Optical Instrumentation Engineers, Washington, 2013. https://doi.org/10.1117/3.883971.ch29.

[34] C. Brosseau, Polarization and the radiation field, in: Fundamentals of Polarized Light: A Statistical Optics Approach, Wiley, 1998. https://books.google.de/books?id=477vAAAAMAAJ.

[35] D. Hipp, A. Mahrle, E. Beyer, Beyond Fresnel: Absorption of fibre laser radiation on rough stainless steel surfaces, Journal of Physics D Applied Physics. 52 (2019) 355302. https://doi.org/10.1088/1361-6463/ab2415.

[36] Y. Li, M. Založnik, J. Zollinger, L. Dembinski, A. Mathieu, Effects of the powder, laser parameters and surface conditions on the molten pool formation in the selective laser melting of IN718, Journal of Materials Processing Technology. 289 (2021) 116930. https://doi.org/10.1016/J.JMATPROTEC.2020.116930.

[37] R.P. Martukanitz, A critical review of laser beam welding, in: Proc.SPIE, 2005. https://doi.org/10.1117/12.601655.

[38] T. Sun, P. Franciosa, M. Sokolov, D. Ceglarek, Challenges and opportunities in laser welding of 6xxx high strength aluminium extrusions in automotive battery tray construction, Procedia CIRP. 94 (2020) 565–570. https://doi.org/10.1016/J.PROCIR.2020.09.076.

[39] N.A. McPherson, K. Chi, T.N. Baker, Submerged arc welding of stainless steel and the challenge from the laser welding process, Journal of Materials Processing Technology. 134 (2003) 174–179. https://doi.org/10.1016/S0924-0136(02)00466-1.

[40] R. Wester, Energy Transport and Heat Conduction, in: R. Poprawe (Ed.), Tailored Light 2: Laser Application Technology, Springer Berlin Heidelberg, Berlin, Heidelberg, 2011: pp. 43–62. https://doi.org/10.1007/978-3-642-01237-2_4.

[41] R. Wester, Absorption of Laser Radiation, in: R. Poprawe (Ed.), Tailored Light 2: Laser Application Technology, Springer Berlin Heidelberg, Berlin,

Heidelberg, 2011: pp. 15–41. https://doi.org/10.1007/978-3-642-01237-2_3.

[42] R. Wester, Melt Flow, in: R. Poprawe (Ed.), Tailored Light 2: Laser Application Technology, Springer Berlin Heidelberg, Berlin, Heidelberg, 2011: pp. 77–91. https://doi.org/10.1007/978-3-642-01237-2_7.

[43] D.H. Abbott, C.E. Albright, CO2 shielding gas effects in laser welding mild steel, Journal of Laser Applications. 6 (1994) 69–80. https://doi.org/10.2351/1.4745339.

[44] P. Kah, A. Salminen, J. Martikainen, The analysis of shielding gases in laser-arc hybrid welding processes, Proceedings of the Institution of Mechanical Engineers, Part B: Journal of Engineering Manufacture. 225 (2011) 1073–1082. https://doi.org/10.1177/2041297510393809.

[45] C. Hagenlocher, J. Lind, J. Wagner, M. Hummel, A. Olowinsky, R. Weber, T. Graf, D.F. G, Comparison of heat conduction mode and deep penetration mode by means of high-speed synchrotron X-ray videos during laser beam welding, Database: DaRUS - Institut Für Strahlwerkzeuge Universität Stuttgart. (2021). https://doi.org/doi/10.18419/darus-2078.

[46] M. Berczeli, G. Buza, Relationship between the keyhole laser welding and the plasma, IOP Conference Series: Materials Science and Engineering. 448 (2018) 012051. https://doi.org/10.1088/1757-899X/448/1/012051.

[47] R. Wester, Laser-Induced Vaporization, in: R. Poprawe (Ed.), Tailored Light 2: Laser Application Technology, Springer Berlin Heidelberg, Berlin, Heidelberg, 2011: pp. 93–111. https://doi.org/10.1007/978-3-642-01237-2_8.

[48] B.R. Finke, P.D. Kapadia, J.M. Dowden, A fundamental plasma based model for energy transfer in laser material processing, Journal of Physics D: Applied Physics. 23 (1990) 643–654. https://doi.org/10.1088/0022-3727/23/6/003.

[49] T. Schmidt, Stand der Wissenschaft und Technik, in: T. Schmidt (Ed.), Potentialbewertung Generativer Fertigungsverfahren Für Leichtbauteile, Springer Berlin Heidelberg, Berlin, Heidelberg, 2016: pp. 17–83. https://doi.org/10.1007/978-3-662-52996-6_3.

[50] E. Kannatey-Asibu, Rapid Prototyping, in: Principles of Laser Materials Processing, John Wiley & Sons, Ltd, 2009: pp. 407–430. https://doi.org/https://doi.org/10.1002/9780470459300.ch19.

[51] C. Over, Rapid Prototyping and Rapid Tooling, in: R. Poprawe (Ed.), Tailored Light 2: Laser Application Technology, Springer Berlin Heidelberg, Berlin, Heidelberg, 2011: pp. 253–263. https://doi.org/10.1007/978-3-642-01237-2_13.

[52] C.K. Chua, K.F. Leong, 3D Printing and Additive Manufacturing, WORLD SCIENTIFIC, 2016. https://doi.org/doi:10.1142/10200.

[53] A. Ulbricht, G. Mohr, S.J. Altenburg, S. Oster, C. Maierhofer, G. Bruno, Can Potential Defects in LPBF Be Healed from the Laser Exposure of Subsequent Layers? A Quantitative Study, Metals (Basel). 11 (2021). https://doi.org/10.3390/met11071012.

[54] W. Liu, K.M. Saleheen, Z. Tang, H. Wang, G. Al-Hammadi, A. Abdelrahman, Z. Yongxin, S.-G. Hua, F. Wang, Review on scanning pattern evaluation in laser-based additive manufacturing, Optical Engineering. 60 (2021) 1–18. https://doi.org/10.1117/1.OE.60.7.070901.

[55] E. Kannatey-Asibu, Sensors for Process Monitoring, in: Principles of Laser Materials Processing, John Wiley & Sons, Ltd, 2009: pp. 407–430. https://doi.org/https://doi.org/10.1002/9780470459300.ch21.

[56] E. Kannatey-Asibu, Processing of Sensor Outputs, in: Principles of Laser Materials Processing, John Wiley & Sons, Ltd, 2009: pp. 407–430. https://doi.org/https://doi.org/10.1002/9780470459300.ch22.

[57] R. Payling, T. Nelis, N.W. Barnett, Glow Discharge Optical Emission Spectroscopy, The Royal Society of Chemistry, 2003. https://doi.org/10.1039/9781847550989.

[58] A. Matsunawa, T. Ohnawa, Beam-Plume Interaction in Laser Materials Processing, Transactions of JWRI. 20 (1991) 9–15. http://hdl.handle.net/11094/11958 (accessed May 8, 2022).

[59] S.S. Harilal, B.E. Brumfield, N.L. LaHaye, K.C. Hartig, M.C. Phillips, Optical spectroscopy of laser-produced plasmas for standoff isotopic analysis, Applied Physics Reviews. 5 (2018) 021301. https://doi.org/10.1063/1.5016053.

[60] G. Peach, Theory of the pressure broadening and shift of spectral lines, Advances in Physics. 30 (1981) 367–474. https://doi.org/10.1080/00018738100101467.

[61] D. Meschede, Laserspektroskopie, in: D. Meschede (Ed.), Optik, Licht Und Laser, Vieweg+Teubner, Wiesbaden, 2008: pp. 407–443. https://doi.org/10.1007/978-3-8348-9288-1_11.

[62] F. Rezaei, G. Cristoforetti, E. Tognoni, S. Legnaioli, V. Palleschi, A. Safi, A review of the current analytical approaches for evaluating, compensating and exploiting self-absorption in Laser Induced Breakdown Spectroscopy, Spectrochimica Acta Part B: Atomic Spectroscopy. 169 (2020) 105878. https://doi.org/10.1016/J.SAB.2020.105878.

[63] A. Ancona, V. Spagnolo, P.M. Lugarà, M. Ferrara, Optical sensor for real-time monitoring of CO2 laser welding process, Applied Optics. 40 (2001) 6019–6025. https://doi.org/10.1364/AO.40.006019.

[64] A.R. Konuk, R.G.K.M. Aarts, A.J.H. t. Veld, T. Sibillano, D. Rizzi, A. Ancona, Process Control of Stainless Steel Laser Welding using an Optical Spectroscopic Sensor, Physics Procedia. 12 (2011) 744–751. https://doi.org/10.1016/J.PHPRO.2011.03.093.

[65] A.R. Konuk, R. Aarts, B.H. in't Veld, T. Sibillano, D. Rizzi, A. Ancona, Closed loop control of laser welding using an optical spectroscopic sensor for Nd:YAG and CO2 lasers, International Congress on Applications of Lasers & Electro-Optics. 2011 (2011) 85–94. https://doi.org/10.2351/1.5062339.

[66] A.R. Konuk, R. Aarts, B.H. in't Veld, Spectral analysis of the process emission during laser welding of AISI 304 stainless steel with disk and Nd:YAG laser, International Congress on Applications of Lasers & Electro-Optics. 2009 (2009) 666–675. https://doi.org/10.2351/1.5061626.

[67] T. Sibillano, A. Ancona, V. Berardi, E. Schingaro, P. Parente, P.M. Lugarà, Correlation spectroscopy as a tool for detecting losses of ligand elements in laser welding of aluminium alloys, Optics and Lasers in Engineering. 44 (2006) 1324–1335. https://doi.org/10.1016/J.OPTLASENG.2005.12.002.

[68] T. Sibillano, A. Ancona, V. Berardi, P. Lugarà, A Real-Time Spectroscopic Sensor for Monitoring Laser Welding Processes, Sensors (Basel). 9 (2009) 3376–3385. https://doi.org/10.3390/s90503376.

[69] W.W. Duley, Control of Laser Welding, in: Laser Welding, John Wiley & Sons Inc, 1998.

[70] W. Eckl, N. Eisenreich, Determination of the Temperature in a Solid Propellant Flame by analysis of emission spectra, Propellants, Explosives, Pyrotechnics. 17 (1992) 202–206. https://doi.org/https://doi.org/10.1002/prep.19920170411.

[71] J. Solé, L. Bausa, D. Jaque, Solid State Lamps, in: An Introduction to the Optical Spectroscopy of Inorganic Solids, John Wiley & Sons, 2005.

[72] J. Solé, L. Bausa, D. Jaque, Thermal Radiation and Planck's Law, in: An Introduction to the Optical Spectroscopy of Inorganic Solids, John Wiley & Sons, 2005.

[73] V. Onuseit, M. Ahmed, R. Weber, T. Graf, Space-resolved Spectrometric Measurements of the Cutting Front, Physics Procedia. 12 (2011) 584–590. https://doi.org/10.1016/j.phpro.2011.03.074.

[74] S.G. Dudeck, Kamerabasierte In-situ-Überwachung gepulster Laserschweißprozesse, Karlsruher Institut für Technologie, 2013. https://doi.org/10.5445/KSP/1000034572.

[75] W. Weingartner, K. Schröder, D. Schuöcker, System for monitoring the focal position in laser material processing, Applied Optics. 40 (2001) 4297–4302. https://doi.org/10.1364/AO.40.004297.

[76] J. Li, Y. Zhang, W. Liu, B. Li, X. Yin, C. Chen, Prediction of penetration based on plasma plume and spectrum characteristics in laser welding, Journal of Manufacturing Processes. 75 (2022) 593–604. https://doi.org/10.1016/J.JMAPRO.2022.01.032.

[77] V. Mamuschkin, A. Haeusler, C. Engelmann, A. Olowinsky, H. Aehling, Enabling pyrometry in absorber-free laser transmission welding through pulsed irradiation, Journal of Laser Applications. 29 (2017) 022409. https://doi.org/10.2351/1.4983515.

[78] T. Lantzsch, M. Traub, T. Westphalen, C. Tenbrock, J.H. Schleifenbaum, Laser powder bed fusion of stainless steel 316L using a combination of high-power diode laser and galvanometer scanner, in: Proc.SPIE, 2021. https://doi.org/10.1117/12.2573128.

[79] J. Schille, L. Schneider, A. Streek, S. Kloetzer, U. Loeschner, High-throughput machining using a high-average power ultrashort pulse laser

and high-speed polygon scanner, Optical Engineering. 55 (2016) 1–10. https://doi.org/10.1117/1.OE.55.9.096109.

[80] A. Streek, P. Regenfuss, H. Exner, High Resolution Laser Melting with Brilliant Radiation, in: 2014 International Solid Freeform Fabrication Symposium, University of Texas at Austin, 2014. https://doi.org/10.13140/2.1.2964.6082.

[81] B. King, A.E.W. Rennie, G.R. Bennett, Comparison of galvanometer and polygon scanning systems on component production rates in selective laser sintering, in: Rapid Design, Prototyping & Manufacturing Conference, 2017.

[82] J. Weber, S. Gutscher, S. Lohmüller, E. Lohmüller, A.A. Brand, Laser-doped selective emitter- Process development and speed-up, in: Proc. 35th Eur. Photovolt. Sol. Energy Conf. Exhib., 2018: pp. 379–384. https://doi.org/10.4229/35thEUPVSEC20182018-2BO.3.6.

[83] J. Xie, S. Huang, Z. Duan, Y. Shi, S. Wen, Correction of the image distortion for laser galvanometric scanning system, Optics & Laser Technology. 37 (2005) 305–311. https://doi.org/10.1016/J.OPTLASTEC.2004.04.012.

[84] J. Zhong, R. Nishida, T. Shinshi, Design and precision tracking control of a high-bandwidth fast steering mirror for laser beam machining, Precision Engineering. 73 (2022) 128–139. https://doi.org/10.1016/J.PRECISIONENG.2021.09.003.

[85] K.L. Wlodarczyk, E. Bryce, N. Schwartz, M. Strachan, D. Hutson, R.R.J. Maier, D. Atkinson, S. Beard, T. Baillie, P. Parr-Burman, K. Kirk, D.P. Hand, Scalable stacked array piezoelectric deformable mirror for astronomy and laser processing applications, Review of Scientific Instruments. 85 (2014) 024502. https://doi.org/10.1063/1.4865125.

[86] J. Zhang, Q. Hu, S. Wang, J. Tao, M. Gou, Digital Light Processing Based Three-dimensional Printing for Medical Applications, Int J Bioprint. 6 (2019) 242. https://doi.org/10.18063/ijb.v6i1.242.

[87] V.I. Yurevich, V.A. Grimm, A.A. Afonyushkin, K. v. Yudin, S.G. Gorny, Optical design and performance of F-Theta lenses for high-power and high-precision applications, in: L. Mazuray, R. Wartmann, A.P. Wood (Eds.), Optical Systems Design 2015: Optical Design and Engineering VI, 2015: p. 96261S. https://doi.org/10.1117/12.2190777.

[88] S.F. Sagan, Optical Systems for Laser Scanners, in: G.E. Stutz (Ed.), Handbook of Optical and Laser Scanning, CRC Press, 2018. https://doi.org/10.1201/9781315218243.

[89] M.G. Lee, G. Kim, C.-W. Lee, S.-H. Lee, Y. Jeon, Design of voice coil motor dynamic focusing unit for a laser scanner, Review of Scientific Instruments. 85 (2014) 045104. https://doi.org/10.1063/1.4869339.

[90] P. Penchev, S. Dimov, D. Bhaduri, Experimental investigation of 3D scanheads for laser micro-processing, Optics & Laser Technology. 81 (2016) 55–59. https://doi.org/10.1016/J.OPTLASTEC.2016.01.035.

[91] G. Eberle, V. Chiron, K. Wegener, Simulation and Realization of a Focus Shifting Unit using a Tunable Lens for 3D Laser Material Processing, Physics Procedia. 41 (2013) 441–447. https://doi.org/10.1016/J.PHPRO.2013.03.100.

[92] A. Nussbaum, GEOMETRICAL OPTICS | Lenses and Mirrors, Encyclopedia of Modern Optics, Five-Volume Set. (2005) 1–11. https://doi.org/10.1016/B0-12-369395-0/00685-0.

[93] G.E. Stutz, Polygonal Scanners: Components, Performance, and Design, in: G.E. Stutz (Ed.), Handbook of Optical and Laser Scanning, CRC Press, 2018. https://doi.org/10.1201/9781315218243.

[94] D.R. Lehmbeck, J.C. Urbach, Image Quality for Scanning and Digital Imaging Systems, in: G.E. Stutz (Ed.), Handbook of Optical and Laser Scanning, CRC Press, 2018. https://doi.org/10.1201/9781315218243.

[95] M.A. Ortega Delgado, A.F. Lasagni, Reducing field distortion for galvanometer scanning system using a vision system, Optics and Lasers in Engineering. 86 (2016) 106–114. https://doi.org/10.1016/J.OPTLASENG.2016.05.016.

[96] C. Ozga, Unseen Possibilities of F-Theta Lenses, Optik & Photonik. 13 (2018) 48–51. https://doi.org/https://doi.org/10.1002/opph.201800015.

[97] Q. Liu, H. Zhu, F. Wang, C. Ding, D. Hu, Design and Optimization of F-Theta Focusing Lens Based on ZEMAX, in: 2021 International Conference of Optical Imaging and Measurement (ICOIM), 2021: pp. 41–44. https://doi.org/10.1109/ICOIM52180.2021.9524395.

[98] L. Reichmann, H.-J. Feige, J. Finster, M. Bening, J. Wunderlich, P. Triebel, H. Bernitzki, U. Schuhmann, Improving laser material processing

objective lenses towards better utilization of high brilliance light sources, in: Proc.SPIE, 2012. https://doi.org/10.1117/12.981341.

[99] A. Liu, K. Li, Thermal lensing mitigation for high power laser processing, in: Proc.SPIE, 2021. https://doi.org/10.1117/12.2578360.

[100] M. Stubenvoll, B. Schäfer, K. Mann, Measurement and compensation of laser-induced wavefront deformations and focal shifts in near IR optics, Optics Express. 22 (2014) 25385–25396. https://doi.org/10.1364/OE.22.025385.

[101] Corning® HPFS® 7979, 7980, 8655 Fused Silica Optical Materials Product Information, Corning Incorporate. (2015).

[102] SCHOTT Zemax glass catalog, Schott. (2017).

[103] B.F. Carneiro de Albuquerque, J. Sasian, F. Luis de Sousa, A.S. Montes, Method of glass selection for color correction in optical system design, Optics Express. 20 (2012) 13592–13611. https://doi.org/10.1364/OE.20.013592.

[104] O. Stenzel, Thin Films, Substrates, and Multilayers, in: O. Stenzel (Ed.), Optical Coatings: Material Aspects in Theory and Practice, Springer Berlin Heidelberg, Berlin, Heidelberg, 2014: pp. 81–113. https://doi.org/10.1007/978-3-642-54063-9_4.

[105] O. Stenzel, Material Aspects in Coating Design, in: O. Stenzel (Ed.), Optical Coatings: Material Aspects in Theory and Practice, Springer Berlin Heidelberg, Berlin, Heidelberg, 2014: pp. 159–183. https://doi.org/10.1007/978-3-642-54063-9_6.

[106] S. Laux, H. Bernitzki, D. Fasold, E. Gittler, F. Schmidt, T. Weyh, G. Wurlitzer, Thorium-free interference coatings for infrared applications, in: Proc.SPIE, 2005. https://doi.org/10.1117/12.625146.

[107] O. Stenzel, Oxide Coatings: Porous and Dense Films, in: O. Stenzel (Ed.), Optical Coatings: Material Aspects in Theory and Practice, Springer Berlin Heidelberg, Berlin, Heidelberg, 2014: pp. 187–208. https://doi.org/10.1007/978-3-642-54063-9_7.

[108] S. Laux, N. Kaiser, H.S. Niederwald, M. Mertin, H. Ehlers, D. Ristau, Broadband antireflection coatings deposited with ion-assisted evaporation, in: Proc.SPIE, 1999. https://doi.org/10.1117/12.360066.

[109] B.W. Woods, S.A. Payne, J.E. Marion, R.S. Hughes, L.E. Davis, Thermomechanical and thermo-optical properties of the LiCaAlF6:Cr3+ laser material, Journal of the Optical Society of America B. 8 (1991) 970–977. https://doi.org/10.1364/JOSAB.8.000970.

[110] I.H. Malitson, A Redetermination of Some Optical Properties of Calcium Fluoride, Applied Optics. 2 (1963) 1103–1107. https://doi.org/10.1364/AO.2.001103.

[111] R. Laiho, M. Lakkisto, Investigation of the refractive indices of LaF3, CeF3, PrF3 and NdF3, Philosophical Magazine B. 48 (1983) 203–207. https://doi.org/10.1080/13642818308226470.

[112] M.J. Dodge, Refractive properties of magnesium fluoride, Applied Optics. 23 (1984) 1980–1985. https://doi.org/10.1364/AO.23.001980.

[113] I.H. Malitson, Refraction and Dispersion of Synthetic Sapphire, J Opt Soc Am. 52 (1962) 1377–1379. https://doi.org/10.1364/JOSA.52.001377.

[114] Y. Nigara, Measurement of the Optical Constants of Yttrium Oxide, Japanese Journal of Applied Physics. 7 (1968) 404–408. https://doi.org/10.1143/jjap.7.404.

[115] O. Medenbach, D. Dettmar, R.D. Shannon, R.X. Fischer, W.M. Yen, Refractive index and optical dispersion of rare earth oxides using a small-prism technique, Journal of Optics A: Pure and Applied Optics. 3 (2001) 174–177. https://doi.org/10.1088/1464-4258/3/3/303.

[116] I.H. Malitson, Interspecimen Comparison of the Refractive Index of Fused Silica, J Opt Soc Am. 55 (1965) 1205–1209. https://doi.org/10.1364/JOSA.55.001205.

[117] M.F. Al-Kuhaili, Optical properties of hafnium oxide thin films and their application in energy-efficient windows, Opt Mater (Amst). 27 (2004) 383–387. https://doi.org/10.1016/J.OPTMAT.2004.04.014.

[118] M. Bischoff, M. Sode, D. Gäbler, H. Bernitzki, C. Zaczek, N. Kaiser, A. Tünnermann, Metal fluoride coatings prepared by ion-assisted deposition, in: Proc.SPIE, 2008. https://doi.org/10.1117/12.797422.

[119] E. Gittler, H. Bernitzki, H. Lauth, Th. Weyh, Novel high-efficiency and cost-effective filters and windows for infrared detectors, in: Proc.SPIE, 2006. https://doi.org/10.1117/12.664883.

[120] Q. Chen, G. Hubbard, P.A. Shields, C. Liu, D.W.E. Allsopp, W.N. Wang, S. Abbott, Broadband moth-eye antireflection coatings fabricated by low-cost nanoimprinting, Applied Physics Letters. 94 (2009) 263118. https://doi.org/10.1063/1.3171930.

[121] K. Prasad, A. Goyal, K. Gohil, I. Jagyasi, Highly reflective coatings, Int J Appl Eng Res. 13 (2018) 15773–15782.

[122] J. Mohelnikova, Materials for reflective coatings of window glass applications, Construction and Building Materials. 23 (2009) 1993–1998. https://doi.org/10.1016/J.CONBUILDMAT.2008.08.033.

[123] F. Rainer, F.P. de Marco, J.T. Hunt, A.J. Morgan, L.P. Mott, F. Marcelja, M.R. Greenberg, High-threshold highly reflective coatings at 1064 nm, in: Proc.SPIE, 1991. https://doi.org/10.1117/12.57235.

[124] P.W. Baumeister, Reflectors, edge filters and periodic structures, in: Optical Coating Technology, Spie Press, 2004.

[125] P.W. Baumeister, Coating deposition, in: Optical Coating Technology, Spie Press, 2004.

[126] P.W. Baumeister, Beamdividers and polarizers, in: Optical Coating Technology, Spie Press, 2004.

[127] P.J. DePond, G. Guss, S. Ly, N.P. Calta, D. Deane, S. Khairallah, M.J. Matthews, In situ measurements of layer roughness during laser powder bed fusion additive manufacturing using low coherence scanning interferometry, Materials & Design. 154 (2018) 347–359. https://doi.org/10.1016/J.MATDES.2018.05.050.

[128] P.A. Hooper, Melt pool temperature and cooling rates in laser powder bed fusion, Additive Manufacturing. 22 (2018) 548–559. https://doi.org/10.1016/J.ADDMA.2018.05.032.

[129] P. Lott, H. Schleifenbaum, W. Meiners, K. Wissenbach, C. Hinke, J. Bültmann, Design of an Optical system for the In Situ Process Monitoring of Selective Laser Melting (SLM), Physics Procedia. 12 (2011) 683–690. https://doi.org/10.1016/J.PHPRO.2011.03.085.

[130] N.V. Tkachenko, Introduction, in: Optical Spectroscopy, Elsevier Science, 2006: pp. 1–14. https://doi.org/10.1016/B978-044452126-2/50025-3.

[131] N.V. Tkachenko, Optics and Optical Devices, in: Optical Spectroscopy, Elsevier Science, 2006: pp. 15–38. https://doi.org/10.1016/B978-044452126-2/50026-5.

[132] M. Capitelli, G. Colonna, G. D'Ammando, R. Gaudiuso, L.D. Pietanza, Physical Processes in Optical Emission Spectroscopy, in: S. Musazzi, U. Perini (Eds.), Laser-Induced Breakdown Spectroscopy: Theory and Applications, Springer Berlin Heidelberg, Berlin, Heidelberg, 2014: pp. 31–57. https://doi.org/10.1007/978-3-642-45085-3_2.

[133] S. Musazzi, U. Perini, LIBS Instrumental Techniques, in: S. Musazzi, U. Perini (Eds.), Laser-Induced Breakdown Spectroscopy: Theory and Applications, Springer Berlin Heidelberg, Berlin, Heidelberg, 2014: pp. 59–89. https://doi.org/10.1007/978-3-642-45085-3_3.

[134] A.M. Malvezzi, Laser–Matter Interaction in LIBS Experiments, in: S. Musazzi, U. Perini (Eds.), Laser-Induced Breakdown Spectroscopy: Theory and Applications, Springer Berlin Heidelberg, Berlin, Heidelberg, 2014: pp. 3–29. https://doi.org/10.1007/978-3-642-45085-3_1.

[135] S. Legnaioli, G. Lorenzetti, L. Pardini, G.H. Cavalcanti, V. Palleschi, Applications of LIBS to the Analysis of Metals, in: S. Musazzi, U. Perini (Eds.), Laser-Induced Breakdown Spectroscopy: Theory and Applications, Springer Berlin Heidelberg, Berlin, Heidelberg, 2014: pp. 169–193. https://doi.org/10.1007/978-3-642-45085-3_7.

[136] S. Hertegård, H. Larsson, T. Wittenberg, High-speed imaging: applications and development, Logopedics Phoniatrics Vocology. 28 (2003) 133–139. https://doi.org/10.1080/14015430310015246.

[137] H. Köhler, On Abbe's Theory of Image Formation in the Microscope, Optica Acta: International Journal of Optics. 28 (1981) 1691–1701. https://doi.org/10.1080/713820514.

[138] G. Indebetouw, A. el Maghnouji, R. Foster, Scanning holographic microscopy with transverse resolution exceeding the Rayleigh limit and extended depth of focus, Journal of the Optical Society of America A. 22 (2005) 892–898. https://doi.org/10.1364/JOSAA.22.000892.

[139] C. Kisielowski, E. Principe, B. Freitag, D. Hubert, Benefits of microscopy with super resolution, Physica B: Condensed Matter. 308–310 (2001) 1090–1096. https://doi.org/10.1016/S0921-4526(01)00896-1.

[140] J.A. Slotwinski, E.J. Garboczi, P.E. Stutzman, C.F. Ferraris, S.S. Watson, M.A. Peltz, Characterization of Metal Powders Used for Additive Manufacturing, J Res Natl Inst Stand Technol. 119 (2014) 460–493. https://doi.org/10.6028/jres.119.018.

[141] G. Eshel, G.J. Levy, U. Mingelgrin, M.J. Singer, Critical Evaluation of the Use of Laser Diffraction for Particle-Size Distribution Analysis, Soil Science Society of America Journal. 68 (2004) 736–743. https://doi.org/https://doi.org/10.2136/sssaj2004.7360.

[142] S.J. Blott, D.J. Croft, K. Pye, S.E. Saye, H.E. Wilson, Particle size analysis by laser diffraction, Geological Society, London, Special Publications. 232 (2004) 63. https://doi.org/10.1144/GSL.SP.2004.232.01.08.

Department of PPU
Division of TVM

ISSN 1402-1757
ISBN 978-91-8048-098-7 (print)
ISBN 978-91-8048-099-4 (pdf)

Print: Lenanders Grafiska, 428782

LULEÅ
UNIVERSITY
OF TECHNOLOGY